Article

A Two-step FE Model Updating Approach for System and Damage Identification of Full-Scale Prestressed Bridge Girders

Niloofar Malekghaini [1], Farid Ghahari [2], Hamed Ebrahimian [3,*], Matthew Bowers [4], Eric Ahlberg [5], Ertugrul Taciroglu [6]

1 Department of Civil and Environmental Engineering, University of Nevada, Reno, NV, U.S. nmalekghaini@nevada.unr.edu
2 Department of Civil and Environmental Engineering, University of California, Los Angeles, CA, U.S. ghahari@seas.ucla.edu
3 Department of Civil and Environmental Engineering, University of Nevada, Reno, NV, U.S. hebrahimian@unr.edu
4 SC Solutions Inc., Sunnyvale, CA, U.S. mbowers@scsolutions.com
5 Department of Civil and Environmental Engineering, University of California, Los Angeles, CA, U.S. eahlberg@ucla.edu
6 Department of Civil and Environmental Engineering, University of California, Los Angeles, CA, U.S. etacir@ucla.edu
* Correspondence: hebrahimian@unr.edu

Abstract: The average age of in-service bridges has increased in recent years in the United States. To address this issue, structural health monitoring and damage identification approaches can be employed to prioritize maintenance/replacement of aging bridges. Among the damage identification and operational health monitoring approaches, finite element (FE) model updating methods can offer a solution to evaluate the mechanics-based characteristics of bridges. However, in a real-world setting, unidentifiability and mutual dependency between model parameters, modeling errors, especially due to boundary conditions, as well as ill-conditioning of updating algorithms can pose challenges to the application of FE model updating methods. To address these challenges, this study presents a two-step FE model updating approach. In the first step, modal-based model updating is used to estimate linear model parameters mainly related to the stiffness of boundary conditions and material properties. In the second step, in order to refine parameter estimation accounting for nonlinear response behavior of the bridge, a time-domain model updating is carried out. In this step, boundary conditions are fixed at their final estimates using modal-based model updating. To prevent the convergence of updating algorithm to local solutions, the initial estimates for nonlinear material properties are selected based on their corresponding final estimates in the modal-based model updating. To validate the applicability of the two-step FE model updating approach, a series of forced-vibration experiments are designed and carried out on a pair of decommissioned and deteriorated prestressed bridge I-girders. After carrying out the two-step FE model updating, the final estimates of concrete compressive strength are shown to provide reasonable assessment of the damage extent in the girders.

Keywords: Modal-based model updating, Bayesian model updating, System identification, Damage identification, Operational health monitoring, I-girder, Bridge, Aging.

1. Introduction

Bridges are vital components of the transportation infrastructure. The average age of in-service bridges in the United States is increasing, which necessitates methods and tools to inform decision making related to maintenance and/or replacement of these structures [1]. Finite Element (FE) model updating methods have emerged as a venerable procedure for operational health monitoring and post-event structural damage identification [2–15]. In these methods, the initial/baseline FE model – developed using available as-built

 doi:10.20944/preprints202212.0282.v1

drawings – is updated using measured dynamic responses. During this process, uncertain model parameters – including material properties, damping parameters, boundary conditions, etc. – are calibrated/estimated. The deviation of final estimates of model parameters from their initial/baseline values reveals information regarding the location and extent of damage in the structure.

FE model updating approaches are mainly divided into two groups. The first group is *modal-based model updating*, wherein the initial FE model is updated to match the identified modal properties of the structure. In this method, the modal properties are first identified using modal identification methods (e.g., [16–20]). Then, the parameters characterizing the linear response behavior of the FE model are estimated to reduce the discrepancies between the identified and FE-predicted modal properties [21]. System and damage identification using modal-based model updating is prone to some challenges. The accuracy of the identified modal signatures is controlled by the level of nonlinearity in the response behavior of structure, measurement noise, excitation frequency range, and sensor sparsity. The uncertainty in the identified modal properties propagates into the model updating process and is reflected in the final estimates of model parameters. In addition, while modal properties are sensitive to the linear model parameters (e.g., elastic modulus of material, support stiffness), they cannot be used to infer parameters characterizing the nonlinear material behavior. The estimates of nonlinear material behavior can be useful to identify local-level and aging-related damage in structures. Consequently, the updated FE model may not be able to predict the dynamic response behavior of the structure correctly, especially when the structure is subjected to material nonlinearity. Although the estimated linear model parameter can be used for structural monitoring and damage identification [22], the application of modal-based model updating for damage identification of reinforced concrete bridges has been shown to be limited [23,24]. The second group of model updating approaches is referred to as *time-domain model updating* [15,25,26]. In this approach, the unknown model parameters characterizing linear and/or nonlinear response behavior of structure are updated to reduce the discrepancies between the measured and FE-predicted responses in time domain. In contrast to the modal-based model updating method, the measured dynamic responses of the structure are used directly for the purpose of model updating in this approach. The direct application of dynamic responses in time-domain model updating eliminates the propagation of modal identification uncertainties into the model updating process.

Several studies in the literature have focused on the system and damage identification of bridges subjected to ambient or traffic excitation (i.e., operational conditions). Modal-based model updating has been used in real-world and laboratory settings using deterministic and stochastic filtering approaches [8,27–31]. The performance of these methods is evaluated by comparing the identified and posterior FE-predicted modal signatures of the studied bridge. The application of time-domain model updating for bridges subjected to traffic excitation has also attracted research interest recently. For example, Abedin et al. in [15], used measured static deformations of a precast prestressed concrete box-girder bridge for model updating to estimate the damage at deck panel joints. The literature also includes studies in which a combination of static responses and modal properties are used to update FE model of bridges, e.g., [4,5,9,32,33]. In general, the number of studies that implement model updating of bridge structures using time-domain measurements under traffic load are scarce.

It is worth noting that static/pseudo-static responses (e.g., displacement measurements) contain limited information regarding the dynamic behavior of the bridge compared to acceleration measurements. The identification of mechanics-based characteristics of the deteriorate bridges using static responses can be challenging. Moreover, unidentifiability and mutual dependency between model parameters, modeling errors, as well as convergence of parameters to local solution may challenge the model updating process [3,34,35]. These challenges are exacerbated in real-world application, especially in cases with large number of uncertain model parameters. To tackle these challenges in real-world applications, a combined modal-based and time-domain model updating can be

 doi:10.20944/preprints202212.0282.v1

used. Based on this, the current study brings the application of model updating to operational health monitoring and damage identification of aged bridges using acceleration responses and introduces a new two-step FE model updating procedure.

In this procedure, first, a deterministic modal-based model updating is carried out to estimate the linear model parameters of a bridge. These model parameters are related to boundary conditions and material properties. Then, in order to refine the parameter estimation and account for nonlinear response behavior of the bridge, a time-domain model updating is carried out. In this step, nonlinear material properties as well as the damping energy-dissipation-related model parameters are estimated while the linear-elastic model parameters are fixed at their final estimates obtained from the modal-based model updating. The final estimates of material properties are used to infer/quantify damage in the bridge. This two-step model updating reduces the following inherent challenges of model updating:

- Unidentifiability and/or mutual dependency between model parameters: this is done through assimilation of linear and nonlinear response behavior of bridge in two steps and estimation of the most sensitive model parameters at each step.
- Convergence to local solution: this is done through setting the initial value of unknown model parameters in time-domain model updating based on the corresponding final estimates from modal-based model updating.
- Uncertainties in boundary conditions: this is done through estimation of related linear-elastic model parameters in the modal-based model updating and fixing these parameters during the time-domain model updating.

To show the two-step FE model updating method and validate its applicability for damage identification in a real-world setting, a pair of full-scale precast prestressed bridge I-girders were used as testbed structures. These girders were in service from 1971 until 2009 before they were decommissioned and repurposed for research experiments [36]. A series of forced-vibration experiments were designed specifically for this study. The girders were subjected to sinusoidal force excitations and their acceleration responses were measured at different locations. First, the collected acceleration responses are used to identify the modal signatures of the testbed structure. Then, the two-step FE model updating is carried out. In the first step, the initial FE model of girders is updated in the modal domain, and boundary conditions, including stiffness of supports and coupling beams, as well as material properties, including initial stiffness of concrete material, are estimated. The updated model is used as the prior model in the Bayesian model updating process to estimate concrete compressive strength and damping properties. Comparison between the posterior FE-predicted responses and field measurements shows a good agreement in the time domain. Moreover, the final estimates of concrete compressive strength result in a realistic damage identification/quantification for the girders. This process validates the applicability of the introduced two-step FE model updating approach for damage identification of bridge structures/components under operational conditions. While the input load used in this study varies from moving traffic load, this study proves the concept for future real-world application.

The paper is organized as follows. Section 2 introduces the testbed structure and the experiments. Section 3 discusses the employed modal identification method and its results. Then, the details of the initial FE model is presented in Section 4. The modal-based model updating and the resulting updated FE model are shown in Section 5. Section 6 discusses the identifiability analysis, methodology, and results of Bayesian model updating. Concluding remarks are presented in Section 7.

2. Description of the field experiment

2.1. Testbed structure

The testbed structure in this study includes two AASHTO precast prestressed bridge I-girders that were part of the Maryland 90 bridge. After decommissioning, the girders were salvaged and transferred to the Turner-Fairbank Highway Research Center

Preprints (www.preprints.org) | NOT PEER-REVIEWED | Posted: 15 December 2022 doi:10.20944/preprints202212.0282.v1

(TFHRC) in McLean, Virginia, to be used as a research testbed [36,37]. The cross-section and elevation views of the girders are shown in Figure 1.

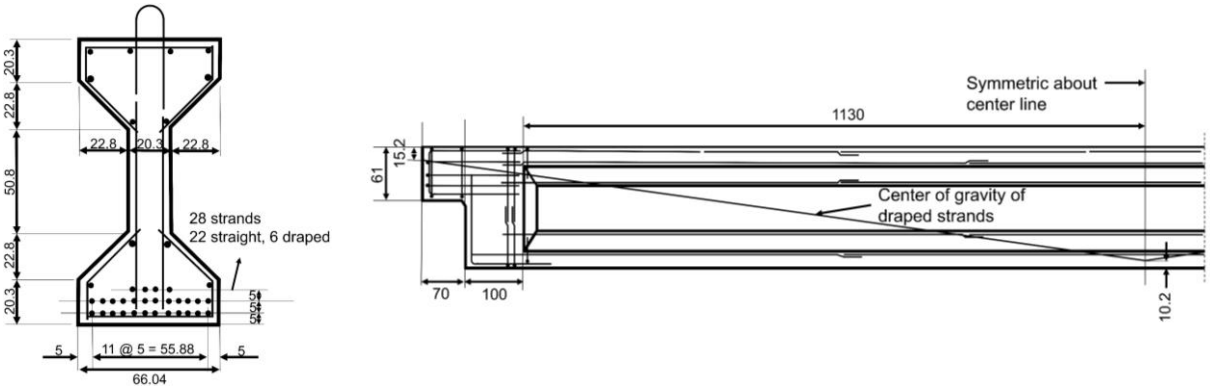

(**a**) (**b**)

Figure 1. The testbed structure: (**a**) cross-section view of each girder, and (**b**) elevation view of each girder. All the dimensions are in centimeters and all reinforcing rebars are #4 (equivalent to Φ13).

The studied girders are 1.37 m deep and 26 m long. Reinforcements and prestressing steel strands are shown in Figure 1. A side view of the testbed structure (with a 20 cm slab on top of each girder) is shown in Figure 2 (a). After being transferred to the TFHRC, each girder was placed on two 1×1 m^2 bearing pads on top of two 2.3×1.6×1.6 m^3 geosynthetic reinforced soil (GRS) piers [38]. These can be seen in Figure 2 (b) and (c). The girders were placed parallel to each other with 2.9 m centerline spacing and were connected with four coupling beams with 0.3×1.4 m^2 cross-sectional area. Three out of four coupling beams are seeable in Figure 2 (d).

The studied girders were in service in a corrosive environment for almost 40 years. The environment simultaneously exposed the concrete matrix of the girders to physical and chemical deterioration processes. Concrete delamination and degradation, as well as steel corrosion, are the main damage mechanisms for concrete bridges in such environment [39]. Due to this, the girders experienced aging and deterioration in several locations, including cracking, steel reinforcement corrosion, spalling, etc. Figure 2 (e) shows an example of the observed damage in girders.

Aside from the aging-related damage discussed above, in 2012, salt spray chambers were installed on each girder to accelerate deterioration in the girders. The chamber installed on the west girder sprayed a 15 weight percent (wt.%) NaCl solution and the chamber installed on the east girder sprayed a 3.5 wt.% NaCl solution. This was part of a study to develop protocols for non-destructive testing (NDT) methods for prestressed girder bridges [36].

(**a**)

Preprints (www.preprints.org) | NOT PEER-REVIEWED | Posted: 15 December 2022 doi:10.20944/preprints202212.0282.v1

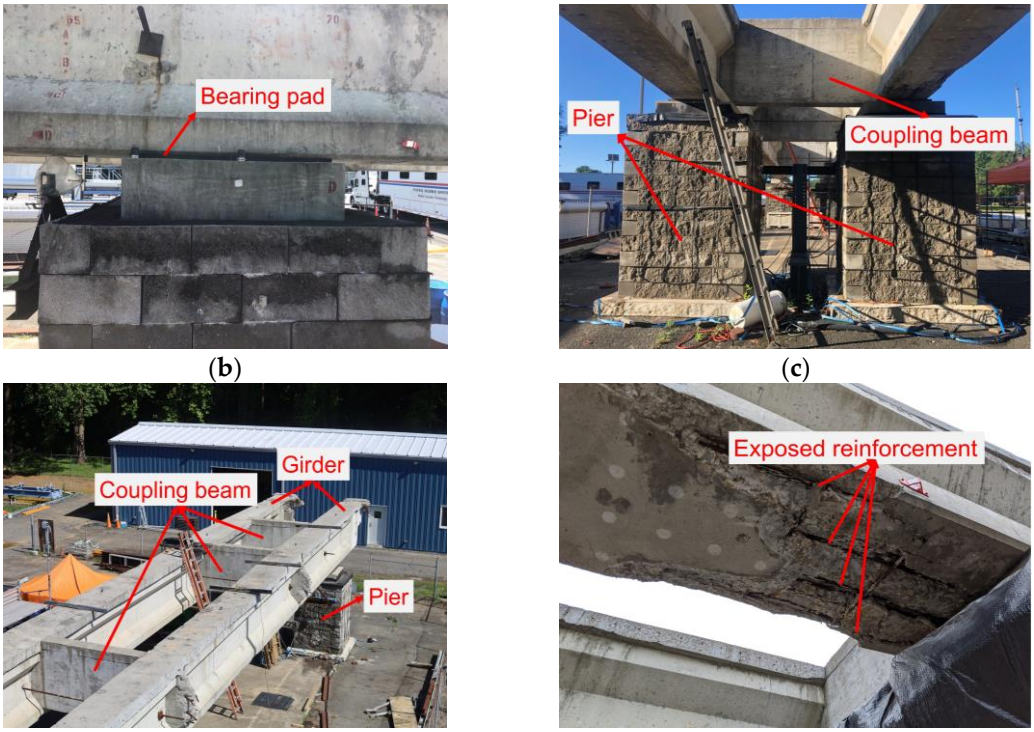

Figure 2. Testbed structure: (**a**) side view and north direction, (**b**) bearing pad, (**c**) piers and coupling beam, (**d**) top view, (**e**) example of existing damage (west girder close to the north pier).

2.2. Dynamic excitation system

The shaker used in this study was a small uniaxial hydraulic device capable of producing arbitrary displacement motions in the vertical direction. The device consisted of a hydraulic piston connected to a servo-hydraulic valve that controlled the motion of a stack of steel plates that combined to form 4450 N of moving weight. The motion was controlled by an MTS PID hydraulic controller using an LVDT sensor to provide feedback displacement. The shaker's hydraulic piston, moving weights, and steel frame of the shaker were supported on four 4450 N load cells, which were used to measure the total force generated by the shaker. The load cells were installed between the shaker plate and the clamping plate on the girder. The shaker plate with dimensions of 30cm×30cm×2cm was located on the top center of the clamping plate with dimensions of 140cm×70cm×5cm (see Figure 3). The shaker displacement and force time histories were collected through a LORD-Microstrain V-Link-200 wireless node [40]. The wireless sensing network is discussed further in the following section. Figure 3 shows a close view of the shaker and Figure 4 shows the two locations (layout 1 and layout 2) at which the shaker was installed on the testbed structure. The hydraulic power for the shaker was provided by a diesel-powered mobile pump.

Figure 3. The shaker installed on the girder.

Preprints (www.preprints.org) | NOT PEER-REVIEWED | Posted: 15 December 2022 doi:10.20944/preprints202212.0282.v1

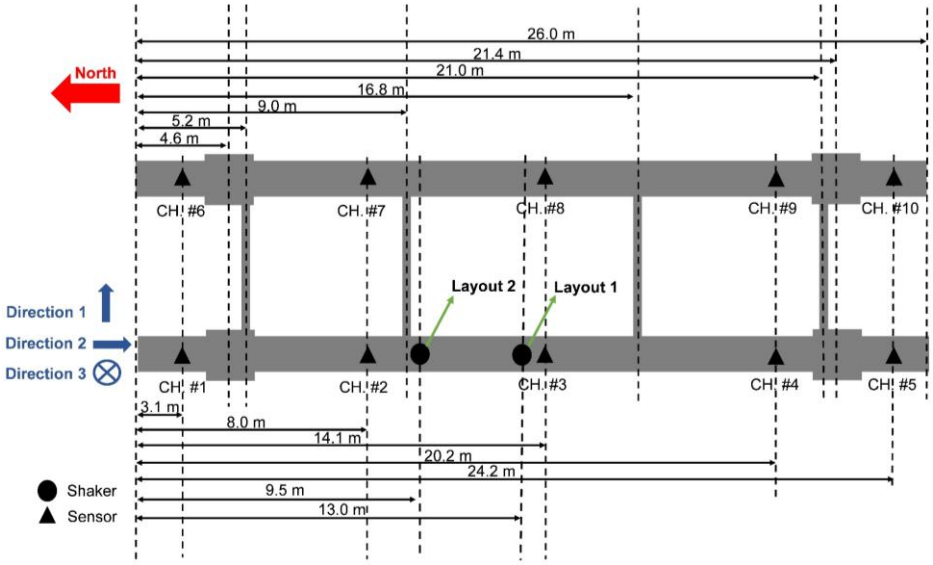

Figure 4. Test layout including the sensor and shaker locations.

2.3. Wireless sensing network

The wireless sensing network included ten battery-powered triaxial MEMS wireless accelerometers (LORD-Microstrain G-Link-200) and a V-Link-200 node [40]. Each accelerometer had an adjustable measurement range of ± 8 g and could be configured for continuous, periodic, or event-triggered sampling modes to output acceleration, tilt, or derived vibration parameters (velocity, amplitude, etc.). The measured data could be transmitted in real-time and/or be saved to the onboard memory with storage capacity up to 8×10^6 data points. The accelerometers had a noise density of 25 $\frac{\mu g}{\sqrt{Hz}}$ with a wireless range up to 1 km and an adjustable sampling rate of up to 4 kHz. Each accelerometer had dimensions of $47\text{mm} \times 43\text{mm} \times 44\text{mm}$. To install the accelerometers, zinc-plated steel washers were glued on top surface of the girders. Then, each accelerometer was screwed to a magnetic base and attached to the washers. Figure 5 shows an installed wireless accelerometer. Data collection and coordination between the wireless nodes, including the accelerometers and the V-Link-200 node, which was used to collect shaker data, were carried out through the wireless USB data acquisition gateway. The gateway used the lossless extended range synchronized (LXRS) data communication protocol and facilitated lossless data collection with node synchronization of ± 50 μs. Synchronization was carried out by transmission of a continuous system-wide timing reference known as the beacon. The communication between the gateway and sensors was wireless through a license-free 2.405 GHz to 2.480 GHz radio frequency with 16 channels. The configuration of the network, data acquisition initialization, and sampling mode selection were managed through the SensorConnect software [41], which was installed on a host computer. The layout of the employed accelerometers is shown in Figure 4. In this study, the sampling rate was 128 Hz and the acceleration data were collected in directions 1 (i.e., east-west) and 3 (i.e., up-down).

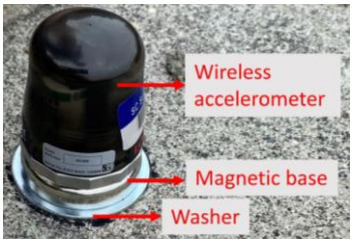

Figure 5. A wireless accelerometer installed on the girder's top surface.

Preprints (www.preprints.org) | NOT PEER-REVIEWED | Posted: 15 December 2022 doi:10.20944/preprints202212.0282.v1

2.4. Forced-vibration testing

The testbed structure was subjected to a series of designed sinusoidal force excitations through frequency sweeps with pre-defined frequency range, duration, and amplitude. Sweeps ranged between 2 Hz to 20 Hz, including 50 different frequencies increasing logarithmically with a duration of 30 seconds for each frequency. Moreover, the sweeps excited the girders with three different target load amplitudes equal to 445 N, 2225 N, and 4450 N. Considering two layouts (see Figure 4) and three levels of load amplitudes, girders were tested under six frequency sweeps. A general view of the testbed structure during the field experiments is shown in Figure 6. The excitation force time history and instantaneous excitation frequency – calculated using a short-time Fourier transform [42] – for each sweep are presented in Figure 7.

Figure 6. The field experiment setup corresponding to layout 2 (See Figure 4).

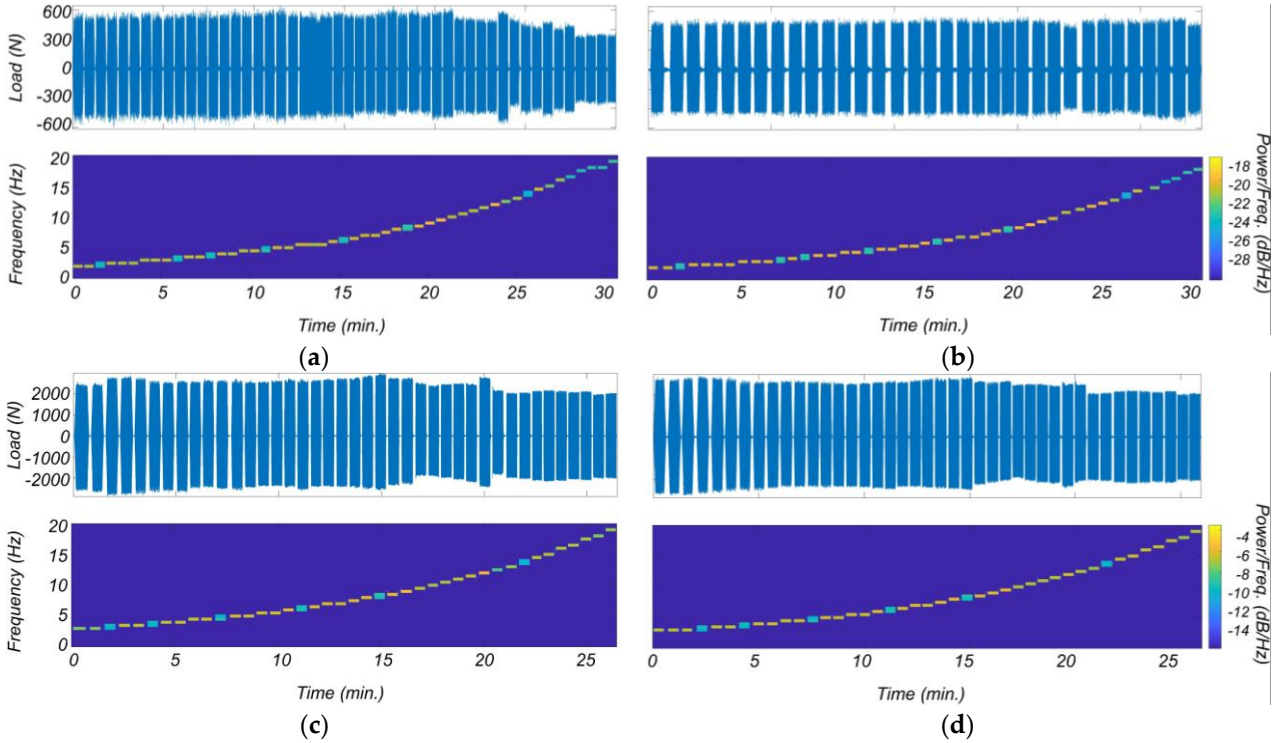

Preprints (www.preprints.org) | NOT PEER-REVIEWED | Posted: 15 December 2022 doi:10.20944/preprints202212.0282.v1

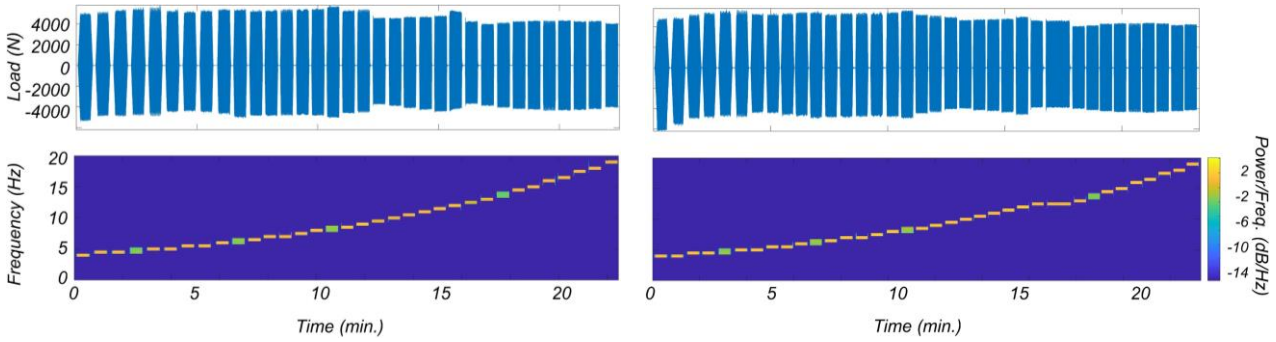

Figure 7. Excitation force time histories and instantaneous excitation frequencies: (**a**) Layout 1 with 445 N target load amplitude, (**b**) Layout 2 with 445 N target load amplitude, (**c**) Layout 1 with 2225 N target load amplitude, (**d**) Layout 2 with 2225 N target load amplitude, (**e**) Layout 1 with 4450 N target load amplitude, and (**f**) Layout 2 with 4450 N target load amplitude.

3. Modal identification

In this section, the modal properties of the testbed structure are identified from the forced-vibration experimental data. For the purpose of modal identification, the collected data from the sweep with layout 1 and 445 N target load amplitude are used (see Figure 7 (a)). This data includes the acceleration of 10 channels in directions 1 and 3 (results in 20 input signals – see Figure 4) and the shaker excitation force. A brief summary of the modal identification process and the identified modal properties are presented in this section.

Various modal identification techniques are available in the literature to identify modal properties – including natural frequencies, damping ratios, and mode shapes – from experimental data [17,19,20]. In this study, due to the nature of the excitation, the empirical frequency response functions (EFRFs) [20] are calculated using applied input (shaker excitation force) and measured outputs (acceleration responses). Then, the calculated multi-output EFRFs are used to estimate a state-space model. This two-stage frequency-domain approach helps to specify the frequency band of interest in which the modal identification needs to be carried out.

The EFRF between a measurement signal $\mathbf{y}(t)$ and input signal $\mathbf{u}(t)$ – depicted by $\mathbf{G}(f)$ – is defined as below:

$$\mathbf{G}(f) = \frac{\mathbf{Y}(f)}{\mathbf{U}(f)} \tag{1}$$

where $\mathbf{Y}(f)$ and $\mathbf{U}(f)$ are Fourier transforms of $\mathbf{y}(t)$ and $\mathbf{u}(t)$, respectively. In a real-world setting, data is always polluted with measurement noise. To reduce the effects of the measurement noise and obtain a smooth EFRF, Welch's averaging method [43] with 12800 data points Hamming window is used for spectral estimation. This size of window is selected to ensure covering full-length of an excitation and the ambient signal before and/or after it.

Having EFRFs for all 20 channels, an n-order state-space model is estimated to fit the estimated EFRFs in the frequency band of interest. In this study, to reduce uncertainties due to low- and high-frequency noises, the frequency band of interest is selected between 2 to 25 Hz. Blue curves in Figure 8 show the calculated EFRFs using measured data.

Preprints (www.preprints.org) | NOT PEER-REVIEWED | Posted: 15 December 2022 doi:10.20944/preprints202212.0282.v1

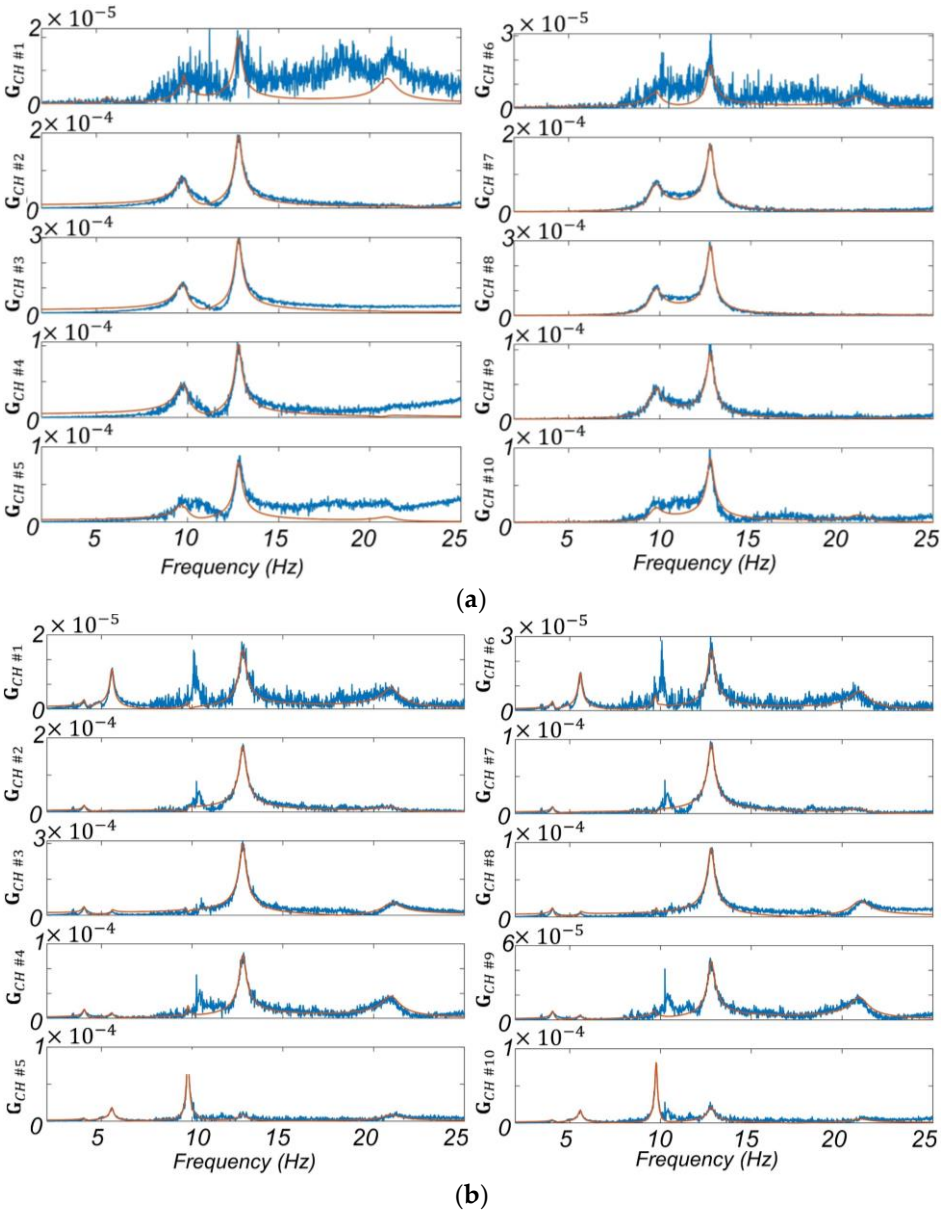

Figure 8. EFRFs calculated from the experimental data (blue) and EFRFs estimated using the identified state-space model (red): (**a**) Direction 3 , and (**b**) Direction 1.

To estimate the state-space model, the subspace state-space identification method is used [44,45]. While this method is briefly explained here, the proof of theory and more details can be found in [44]. In the subspace state-space identification method, measurements are placed in a block Hankel matrix which is divided into a past and a future part. The identification algorithm proceeds with projecting the future measurements into the past measurements while the projection matrix can be factorized as the product of an observability matrix and a state sequence. These two matrices are identified by applying the singular value decomposition (SVD) to the projection matrix and the order of the system is calculated as the number of non-zero singular values. By applying one block shift in separation between past and future measurements in the Hankel matrix, another projection matrix, shifted observability, and state sequence matrices can be obtained. At this point, the system matrices can be calculated from the overdetermined set of linear equations.

The numerical algorithm for system identifications are available in Matlab *n4sid* [46] function and are used in this study. As a classical remedy, the modal identification is carried out for a range of model orders and a stability diagram is plotted on which true modes appear as stable modes [47]. For this purpose, the stability analysis is run considering

Preprints (www.preprints.org) | NOT PEER-REVIEWED | Posted: 15 December 2022 doi:10.20944/preprints202212.0282.v1

model orders from 2 to 40 with 1% and 5% error tolerances for natural frequency and damping ratios, respectively. The stability analysis showed that a model order of $n = 26$ is the lowest model order to have all stable modes within the frequency band of interest. The fits between estimated and calculated EFRFs can be improved using prediction error minimization algorithm and nonlinear least-squares objective functions. This approach is carried out using Matlab *ssest* function [48], which initializes the model parameters based on the previously estimated state-space model, and then updates the parameters using an iterative search to minimize the prediction errors [19]. Red curves in Figure 8 display EFRFs of the estimated state-space model at measurement points. As can be seen, the estimated state-space model is able to approximate the calculated EFRFs acceptably. Identified natural frequencies (f^{ID}) and damping ratios (ξ^{ID}) of the system are reported in Table 1. The identified mode shapes – those which will be used for modal-based model updating – are later shown in Section 5.

Table 1. Identified natural frequencies and damping ratios.

	Mode number					
	1 (Tr*)	2 (Tr)	3 (V**)	4 (Tr)	5 (V)	6 (To***)
$f^{ID}(Hz)$	4.07	5.57	9.73	9.76	12.79	20.98
$\xi^{ID}(\%)$	1.92	1.78	2.97	0.60	1.39	2.18

*: Transverse mode, **: Vertical mode, ***: Torsional mode

4. Finite element modeling of the testbed structure

The initial FE model of the testbed structure is developed in OpenSees [49] using the available as-built drawings. The girders are modeled using fiber-section force-based beam-column elements (*forceBeamColumn*) with approximately 30 cm length and three integration points. Moreover, the linear-elastic shear stiffness and torsional stiffness are aggregated to the fiber sections. The slab is also modeled using rectangular fiber sections as a part of the girders' sections. To model the profile of the draped strands – with a nominal cross-sectional area of 1 cm^2– the strands' depth at the integration points of each element is calculated based on Figure 1. The strand is modeled using a single fiber at its corresponding depth. Girders' concrete material is modeled with nominal compressive strength ($f'_{c,E}$ and $f'_{c,W}$ for the east and west girders) of 46 MPa, strain at maximum strength (ε_c), and strain at crushing strength (ε_u) of 0.2% and 0.5%, respectively. As girders are already damaged, no tensile strength is assumed and therefore, *Concrete01* material model is employed. To model the shear and torsional stiffness of the girder sections, the shear modulus (G) is calculated based on the concrete modulus of elasticity, E ($= E_E = E_W$), and Poisson's ratio of 0.2. The parameters E_E and E_w – modulus of elasticity for the east and west girders – are set equal to the initial slope in *Concrete01* model (i.e., $\frac{2f'_{c,E}}{\varepsilon_c}$ and $\frac{2f'_{c,W}}{\varepsilon_c}$) which is 46 GPa here. Steel is modeled using bilinear *steel01* material with a modulus of elasticity of 200 GPa, and yielding strength of 455 MPa and 1720 MPa for reinforcing steels and strands, respectively. Moreover, the prestressing force in strands (128.60 kN per strand) is modeled by applying its resulting initial strain to the steel material. For this purpose, the normal strain in strands' steel resulting from the prestressing force is calculated by dividing the prestressing force by strand's axial rigidity (product of the strand's modulus of elasticity and gross section area). The calculated strain (0.65%) is assigned to the strands' *steel01* material using *InitStrainMaterial*. The mass and weight of the girders are assigned to the element nodes.

Coupling beams are modeled using *elasticBeamColumn* elements considering the gross cross-sectional area and an *Elastic* material with the modulus of elasticity equal to 30 GPa. The coupling beams are connected to the girders assuming rigid connections. The mass and weight of the coupling beams are assigned to the element nodes. To model each support, the girder nodes that are located along the bearing pad are constrained to a node

Preprints (www.preprints.org) | NOT PEER-REVIEWED | Posted: 15 December 2022 doi:10.20944/preprints202212.0282.v1

at the center of the bearing pad using *rigidLink* constraint. To account for flexibility in the piers and bearing pads, supports are defined using a 6 degrees of freedom (DOFs) spring. This is modeled using *ZeroLength* elements with *Elastic* uniaxial material. Moreover, the energy dissipation in the piers and bearing pads is collectively modeled using a dashpot in the vertical direction. This is done using *ZeroLength* elements with *Viscous* uniaxial material. The corresponding stiffness and damping parameters are initially selected based on engineering judgment [38,50] and are later updated using modal-based and time-domain model updating. The list of model parameters that are later treated as unknown parameters in Sections 5 and 6 and their initial values are summarized in Table 2. In this table, the equivalent values for concrete compressive strength and modulus of elasticities of girders are shown in a same row separated with '/'. The directions in this table are based on Figure 4.

The nonlinear time history analysis is performed using the Newmark average acceleration method with a constant time step size of 0.0078 seconds equal to the measurement sampling rate. The Newton-Raphson method is used to iteratively solve the nonlinear equilibrium equations [51]. To define energy dissipation in the structural system aside from the material nonlinearity, modal damping is modeled for the first six modes. The damping ratios, i.e. $\xi_i \ , \forall\, i \in \{1,2,3,4,5,6\}$, are set equal to the identified ones (see Table 1). The only exceptions are damping ratios for modes 1 and 2 which are set equal 0.02. The reason is to have similar initial values – which is not very different from the identified values (0.0192 and 0.0178) – during time-domain model updating which will be discussed later.

Table 2. Model parameters for the initial FE model. The directions in this table are based on Figure 4.

Parameter	Parameter description	Initial values
$f'_{c,W}$ / E_W	Concrete compressive strength/Concrete modulus of elasticity for the west girder	46 MPa / 46 GPa
$f'_{c,E}$ / E_E	Concrete compressive strength/Concrete modulus of elasticity for the east girder	46 MPa / 46 GPa
E_c	Modulus of elasticity for coupling beams	30 GPa
K_R	Rotational stiffness of bearing pads about directions 1 and 2 and 3	9.4×10^5 kN/rad
K_V	Vertical stiffness of bearing pads in direction 3	1.2×10^5 kN/m
K_T	Transverse stiffness of bearing pads in direction 1	1.6×10^4 kN/m
K_L	Longitudinal stiffness of bearing pads in direction 2	1.6×10^4 kN/m
C_D	Damping coefficient for bearing pads in direction 3	45×10^2 kN. sec/m
ξ_1	Damping ratio for mode 1	0.02
ξ_2	Damping ratio for mode 2	0.02

5. First step: modal-based model updating

The modal properties of the initial FE model are different from the identified ones (Figure 9). Hence, the initial FE model needs to be updated using modal-based model updating to better fit the identified modal properties. As mentioned before, the modal-based model updating is limited to the linear response behavior of structures. Hence, only the linear model parameters are updated at this step. Modal-based model updating process is discussed next.

The modal-based model updating is a process to minimize the discrepancies between identified and FE-predicted modal frequencies and mode shapes through updating the linear parameters of the FE model [22,52]. In this process, an objective function, $g(\boldsymbol{\theta})$, is defined as shown in Eq. (2). The discrepancies between modal frequencies, mode shapes, and a regularization term are respectively the first, second, and third terms in Eq. (2).

Preprints (www.preprints.org) | NOT PEER-REVIEWED | Posted: 15 December 2022 doi:10.20944/preprints202212.0282.v1

$$g(\boldsymbol{\theta}) = W_f\ \mathbf{r}_f{}^T\ \mathbf{r}_f + W_M \left(N - \sum_{i=1}^{i=N} MAC_i \right) + (\boldsymbol{\theta} - \boldsymbol{\theta}_0)^T\ W_\theta\ (\boldsymbol{\theta} - \boldsymbol{\theta}_0) \quad (2)$$

In Eq. (2), the parameter W_f is the weighing scalar for frequency residuals and the term $\mathbf{r_f} \in \mathbb{R}^{\boldsymbol{N\times 1}}$ is the vector including the square root of normalized differences between FE-predicted and identified modal frequencies. The parameter W_M is the weighing scalar for modal assurance criteria (MAC) residuals. The term N is the total number of identified modes that are used for model updating, and the term MAC_i indicates the MAC value for mode i. The parameter W_θ is the weighing scalar for penalizing large deviation of the unknown FE model parameters from their initial values. The vector $\boldsymbol{\theta} \in \mathbb{R}^{n_{\theta M}\times 1}$ is the vector of unknown FE model parameters and $n_{\theta M}$ is the number of unknown model parameters for modal-based model updating. The vector $\boldsymbol{\theta}_0 \in \mathbb{R}^{n_{\theta M}\times 1}$ is the initial estimates of the unknown model parameters. The i^{th} entry of the vector $\mathbf{r}_f$, denoted as $\mathbf{r}_{f,i}$, is defined as follow:

$$\mathbf{r}_{f,i} = \sqrt{\left|\frac{f_i^{ID} - f_i^{FE}}{f_i^{ID}}\right|} \qquad i = 1,2,\dots,N \quad (3)$$

In the above equation, the terms f_i^{ID} and f_i^{FE} are the modal frequencies of the i^{th} identified and FE-predicted modes. The term MAC_i is defined as follow:

$$MAC_i = \frac{|(\boldsymbol{\psi}_i^{ID})^T\ \boldsymbol{\psi}_i^{FE}|^2}{((\boldsymbol{\psi}_i^{ID})^T\ \boldsymbol{\psi}_i^{ID})\ ((\boldsymbol{\psi}_i^{FE})^T\ \boldsymbol{\psi}_i^{FE})} \quad (4)$$

The terms $\boldsymbol{\psi}_i^{ID}$ and $\boldsymbol{\psi}_i^{FE} \in \mathbb{R}^{NDOF\times 1}$ are the i^{th} identified and FE-predicted mode shape vectors, respectively, and $NDOF$ is the number of DOFs. The superscript T denotes matrix/vector transpose operator.

To update the FE model using modal-based model updating, the stiffness-related model parameters E $(= E_E = E_W)$, E_c, K_R, K_V and K_T are selected as unknown FE model parameters to be updated ($n_{\theta M} = 5$). Note that parameter K_L is not selected as there is no measurement in the longitudinal direction of the girders. The vector $\boldsymbol{\theta}_0$ is initiated using the initial values listed in Table 2.

The first two lateral and the first two vertical identified modes ($N = 4$) are used for the modal-based model updating. This is because the first two identified vertical modes are the only ones with frequencies less than 20 Hz (maximum excitation frequency). As can be seen in Figure 4, measurements are collected in 5 vertical (i.e., in direction 3) and 5 lateral (i.e., in direction 1) DOFs for each girder; therefore, $NDOF = 20$. The terms W_f, W_M and W_θ are selected equal to 4, 1, and 0.01 to balance the contributions of the MAC value and frequency errors in the objective function. As a result, the difference between identified and estimated modal frequencies will be penalized more than mode shapes [52]. This is because that the uncertainty in identified mode shapes are greater than frequencies. The constrained nonlinear multivariate optimization function *fmincon* within the Matlab Optimization Toolbox is used [53] with the interior-point algorithm [54]. The maximum iteration number is set to 30, and the process terminates when the relative difference between successive values of the objective function is lower than a given threshold of 10^{-4}. Moreover, the lower and upper bounds for parameter estimation are set equal to $10^{\pm 4}$ times of the initial values.

Comparison between the identified, initial, and updated modal properties is shown in Figure 9 and the updated values for the FE model parameters are shown in Table 3. It is noteworthy that as parameters $E_E = E_W$ are updated, the parameters $f'_{c,E} = f'_{c,W}$ are also updated (using $E_E = \frac{2f'_{c,E}}{\varepsilon_c}$ and $E_W = \frac{2f'_{c,W}}{\varepsilon_c}$ assuming fixed value for ε_c). These equivalent values for each girder are shown in a same column in Table 3 and are separated using '/'. A comparison between Table 2 and Table 3, shows that the parameters E_E and E_W are estimated to a smaller value than their initial ones. This was expected as both girders are aged and have experienced severe damage. The parameter E_c is estimated to a smaller value than its initial one. This is probably due to the presence of cracks in the section and could also be an indication to the fact that the connections between the girders and coupling beams are not completely rigid. The parameters K_R, K_V and K_T are estimated to values greater than their initial ones, which indicates that the bearing pads are

Preprints (www.preprints.org) | NOT PEER-REVIEWED | Posted: 15 December 2022 doi:10.20944/preprints202212.0282.v1

stiffer than what considered in the initial model. The improvement in the modal frequencies are superior to the MAC values. This means that the modal-based model updating process compensates for the frequency match with MAC values. The maximum error in frequency is at the second lateral mode which is less than 8% and is acceptable. The updated model is later used as the prior FE model for the time-domain model updating.

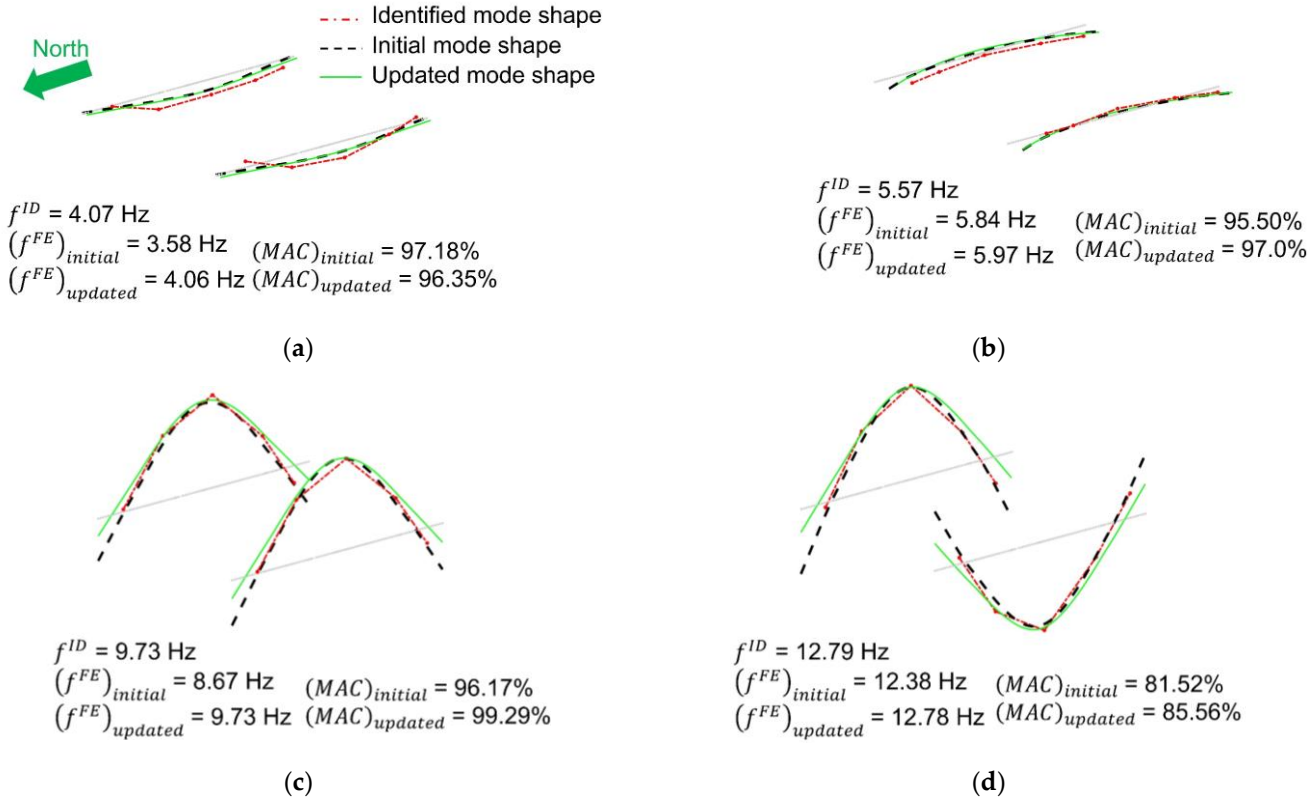

Figure 9. Comparison between identified, initial, and updated modal properties: (**a**) first lateral mode, (**b**) second lateral mode, (**c**) first vertical mode, and (**d**) second vertical mode.

Table 3. The updated FE model parameters after modal-based model updating.

Parameter	$f'_{c,W}/E_W$	$f'_{c,E}/E_E$	E_c	K_R	K_V	K_T
Updated value	39 MPa/39 GPa	39 MPa/39 GPa	28.23 GPa	1.4×10^6 kN/rad	1.8×10^5 kN/m	2.2×10^4 kN/m

6. Second step: time-domain model updating

To this point, the initial FE model of the studied girders is updated using modal-based model updating. It is noteworthy that concrete material has nonlinear response behavior even under small levels of excitation. In addition to that, presence of prestressing force pushes the concrete material across the section along its nonlinear response curve. Then, the applied excitation – shaker force here and traffic load in operational conditions – results in small loading/unloading of concrete material in nonlinear range of response curve. The level of nonlinearity in the response behavior of concrete material increases as a function of deterioration and damage [55]. However, the nonlinear response behavior of the studied girders is not captured through modal-based model updating.

To account for nonlinear response behavior of girders as well as refining the estimation of damage-related model parameters, time-domain model updating – referred here as the second step of model updating procedure – is carried out. The cumulative damage effects in a reinforced concrete section can be modeled by altering the stress-strain

Preprints (www.preprints.org) | NOT PEER-REVIEWED | Posted: 15 December 2022 doi:10.20944/preprints202212.0282.v1

response behavior of the concrete material, e.g., reduction of the effective compressive strength [56–58]. Based on this, it is intended to estimate concrete compressive strengths of girders using time-domain model updating. Moreover, the acceleration measurements contain information regarding the dynamic behavior of the testbed structure. Hence, the energy-dissipation-related model parameters can also be estimated using time-domain model updating. For this purpose, first, the most identifiable FE model parameters are selected using an information-theoretic identifiability analysis [59]. Then, these parameters are updated using the Bayesian model updating process.

6.1. Identifiability analysis for time-domain model updating

The identifiability analysis is an approach to determine the most identifiable unknown model parameters using the sensitivity of FE-predicted responses with respect to the unknown model parameters. In this method, the relative information that each candidate model parameter gains from the responses and the mutual information gain between these parameters are calculated. The model parameters with high relative information gain and little dependency on other parameters are likely more identifiable than others and are selected to be updated in the model updating process.

The data used for identifiability analysis is noted as Data 1-2 in Table 4 which corresponds to layout 1 and the target load amplitude of 2225 N. It is noteworthy that no significant difference is expected in the identifiability analysis results using different layouts and target load amplitudes. However, the target load amplitude for identifiability analysis is selected high enough to have moderate level of loading/unloading response behavior in the concrete material of testbed structure. The data in Table 4 will later be used for model updating.

As can be seen in Table 4, the identifiability analysis and model updating process are performed using experiments with excitation frequencies of 9.73 Hz and 12.86 Hz. These excitation frequencies are selected as they are the closest ones to the identified modal frequencies (9.73 Hz and 12.79 Hz) and are expected to provide useful information on the dynamic behavior of the testbed structure. Moreover, the measured signal-to-noise ratio in the experiments with these frequencies is higher than the similar ratio in experiments with excitation frequencies far from the identified modal frequencies. Higher measured signal-to-noise ratio results in more stable parameter estimation [60].

Table 4. Field experimental data used for the Bayesian FE mode updating. The measured data with excitation frequencies close to mode 1 and mode 2 are lumped together.

Data I.D.	Layout	Target load amplitude	Excitation frequencies	Data I.D.	Layout	Target load amplitude	Excitation frequencies
1-1	1	445N	9.73 Hz and 12.86 Hz	2-1	2	445N	9.73 Hz and 12.86 Hz
1-2	1	2225N	9.73 Hz and 12.86 Hz	2-2	2	2225N	9.73 Hz and 12.86 Hz
1-3	1	4450N	9.73 Hz and 12.86 Hz	2-3	2	4450N	9.73 Hz and 12.86 Hz

Each data set in Table 4 augments two experiments with excitation frequencies of 9.73 Hz and 12.86 Hz (while the layout and target load amplitude are similar). This is shown in the following equations:

$$\mathbf{y} = \begin{bmatrix} \mathbf{y}_{9.73\ \mathrm{Hz}} \\ \mathbf{y}_{12.86\ \mathrm{Hz}} \end{bmatrix} \tag{5}$$

$$\mathbf{u} = \begin{bmatrix} \mathbf{u}_{9.73\ \mathrm{Hz}} \\ \mathbf{u}_{12.86\ \mathrm{Hz}} \end{bmatrix} \tag{6}$$

The terms $\mathbf{y} \in \mathbb{R}^{20\times t_e}$ and $\mathbf{u} \in \mathbb{R}^{2\times t_e}$ denote the acceleration measurements and input excitations that are being used for identifiability analysis and time-domain model updating. The terms $\mathbf{y}_{9.73\ \mathrm{Hz}} \in \mathbb{R}^{10\times t_e}$ and $\mathbf{y}_{12.86\ \mathrm{Hz}} \in \mathbb{R}^{10\times t_e}$ refer to the collected acceleration measurements (at 10 measurement channels in direction 3) from experiments with input excitation frequencies of 9.73 Hz and 12.86 Hz. The terms $\mathbf{u}_{9.73\ \mathrm{Hz}} \in \mathbb{R}^{1\times t_e}$ and

Preprints (www.preprints.org) | NOT PEER-REVIEWED | Posted: 15 December 2022 doi:10.20944/preprints202212.0282.v1

$\mathbf{u}_{12.86\,\mathrm{Hz}} \in \mathbb{R}^{1\times t_e}$ refer to the input excitations with frequencies of 9.73 Hz and 12.86 Hz. The term t_e is the total length of collected data.

One of the intentions of identifiability analysis/time-domain model updating is to analyze the identifiability/update the unknown model parameters ξ_1 and ξ_2. For this purpose, it is required to implement measurements from both excitation frequencies equal to 9.73 Hz and 12.86 Hz. The augmenting process provides measurements that contain dynamic response behavior of the testbed from both its vertical modes.

Parameters $f'_{c,W}$, $f'_{c,E}$, E_c, K_R, K_V, K_L, C_D, ξ_1 and ξ_2 are selected as candidate unknown model parameters. It is intended to refine the damage state estimation of girders for the west and east girder separately. So, the concrete compressive strengths of the west and east girders are modeled using two different parameters $f'_{c,W}$ and $f'_{c,E}$, respectively. While the main intention of the time-domain model updating is to update the model parameters related to the energy dissipation and nonlinear behavior of the structure, the parameters E_c, K_R, K_V and K_L are also considered as candidate unknown parameters. As will be seen later, this is to highlight how the introduced two-step model updating helps with unidentifiability and mutual dependencies between the model parameters. Since the input load mainly excites the first two vertical modes of the girders, the modal damping ratios of these two modes are included in the list of candidates for unknown parameters. The value for parameters $f'_{c,W}$, $f'_{c,E}$, E_c, K_R, and K_V are set equal to their final estimates in modal-based model updating (see Table 3). As the input load is in the vertical direction, the parameter K_T is most probably not identifiable and is excluded from the list of candidate model parameters. The value of parameter K_L is set equal to the updated value of K_T (after modal-based model updating) as the properties of bearing pads are assumed to be the same in the transverse and longitudinal directions. The value of parameters C_D, ξ_1 and ξ_2 are set equal to their initial values (see Table 2), as these parameters were not updated using modal-based model updating.

The relative information gain of the candidate unknown model parameters and relative mutual information gain between the candidate unknown model parameter pairs are shown in Figure 10. As can be seen in this figure, although the parameters E_c, K_R, K_V, K_L have considerable levels of relative information gain, they are highly dependent on the parameters $f'_{c,W}$ and $f'_{c,E}$. This dependency is likely because all these parameters contribute to the stiffness of the testbed structure. Based on this, parameters E_c, K_R, K_V, and K_L are most probably not identifiable together with parameters $f'_{c,W}$ and $f'_{c,E}$. Parameters E_c, K_R, K_V and K_L reflects the linear-elastic response behavior of the testbed structure and are already estimated using modal signatures. Moreover, the parameters $f'_{c,W}$ and $f'_{c,E}$ have relatively large information gain and their estimation is of main interests in time-domain model updating as their final estimates help to refine the damage estimation in girder level and reflect the cumulative damage status of each girder. Hence, parameters $f'_{c,W}$ and $f'_{c,E}$ are selected to be estimated using time-domain model updating while parameters E_c, K_R, K_V and K_L are fixed at their corresponding values in Table 3 obtained from the modal-based model updating. This reduces the challenges of model updating due to the unidentifiability and/or mutual dependencies between model parameters. It is noteworthy that the final estimates of parameters $f'_{c,W}$ and $f'_{c,E}$ using time-domain model updating will inherently be dependent on the fixed values selected for parameters E_c, K_R, K_V, and K_L. Parameters ξ_1, ξ_2, and C_D have relatively moderate information gain and have negligible dependency on other parameters. However, parameter C_D is dependent on parameters ξ_1 and ξ_2 as all of them contribute to the viscous damping energy dissipation of the structure. As the initial value for parameter C_D is selected based on judgment, it is of interest to update this parameter using the model updating process. But, the final estimates of parameters ξ_1, ξ_2 and C_D are expected to vary between different case studies and depend on each other. So, the overall damping of the testbed will be calculated at the end. Based on the above discussion, parameters $f'_{c,W}$, $f'_{c,E}$, ξ_1, ξ_2, and C_D are selected to be estimated using the time-domain model updating.

Preprints (www.preprints.org) | NOT PEER-REVIEWED | Posted: 15 December 2022 doi:10.20944/preprints202212.0282.v1

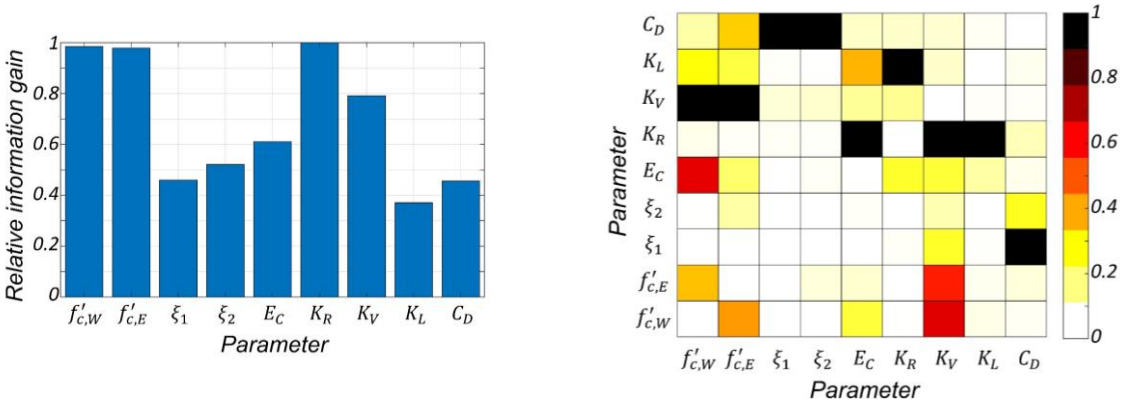

(**a**) (**b**)

Figure 10. Identifiability analysis results: (**a**) relative information gain of the candidate unknown model parameters, (**b**) relative mutual information gain between the candidate unknown model parameter pairs. Each row is normalized to its diagonal value. Then, the diagonal values are nullified.

6.2. Bayesian inference

In the Bayesian model updating, the unknown FE model parameter vector is considered as a random vector with joint probability density function (PDF) whose mean (referred to as estimate hereafter) and covariance are updated recursively through the integration of the FE-predicted and measured responses. The unknown FE model parameters are updated using measured responses in successive overlapping windows. In this approach, known as the sequential estimation window approach [61], the *a priori* estimates of the unknown FE model parameters at each estimation window are updated to the *a posteriori* estimates. A brief review of this method is provided in the following.

Assuming zero-mean Gaussian white noise processes for the measurement noise ($\boldsymbol{\lambda}$) and the process noise ($\mathbf{q}$), the state-space model at each estimation window is set up as follows:

$$\boldsymbol{\vartheta}_{w+1} = \boldsymbol{\vartheta}_w + \mathbf{q}_w \tag{7}$$

$$\mathbf{y}_w = \mathbf{h}_w(\boldsymbol{\vartheta}_w, \mathbf{u}_w) + \boldsymbol{\lambda}_w \tag{8}$$

As can be seen in Eq. (7), the unknown FE model parameter vector for Bayesian model updating, $\boldsymbol{\vartheta} \in \mathbb{R}^{n_{\vartheta_{B_{FE}}} \times 1}$, evolves linearly in the state equation by a random walk process. The term $n_{\vartheta_{B_{FE}}}$ is the number of unknown FE model parameters in the Bayesian model updating. In this study, the term $n_{\vartheta_{B_{FE}}}$ is equal to 5 (which counts the number of parameters $f'_{c,W}$, $f'_{c,E}$, ξ_1, ξ_2, and C_D) and the initial values for the unknown model parameters are equal to those described in the previous section. In Eq. (8), the term $\mathbf{y}_w \in \mathbb{R}^{(n_y \times t_w) \times 1}$ denotes the measurement vector and $\mathbf{h}_w(.) \in \mathbb{R}^{(n_y \times t_w) \times 1}$ denotes the nonlinear FE-predicted response function at the w^{th} estimation window, which spans between time steps $t_{w,1}$ and $t_{w,2}$ with t_o time steps overlap with the previous estimation window. The parameter n_y (here 20) is the number of collected signals and t_w is number of time steps at the w^{th} estimation window. The term $\mathbf{u}_w \in \mathbb{R}^{t_{w,2} \times 1}$ is the deterministic input vector at the w^{th} estimation window. In this study, estimation windows have the length of 150 time steps with 50 time steps overlap, i.e., $t_{1,2}$ =50 and t_w =150 and $t_{w-1,2} - t_{w,1}$ =50 $\forall\, w \geq 2$.

The measurement equation (Eq. (8)), is linearized using the first-order Taylor series expansion with linearization point at the *a priori* estimate. The following equation is obtained:

$$\mathbf{y}_w \cong \mathbf{h}_w\left(\hat{\boldsymbol{\vartheta}}_w^-, \mathbf{u}_w\right) + \frac{\partial \mathbf{h}_w(\boldsymbol{\vartheta}_w, \mathbf{u}_w)}{\partial \boldsymbol{\vartheta}_w}\Big|_{\boldsymbol{\vartheta}_w = \hat{\boldsymbol{\vartheta}}_w^-}\left(\boldsymbol{\vartheta}_w - \hat{\boldsymbol{\vartheta}}_w^-\right) + \boldsymbol{\lambda}_w \tag{9}$$

Preprints (www.preprints.org) | NOT PEER-REVIEWED | Posted: 15 December 2022 doi:10.20944/preprints202212.0282.v1

in which the superscripts –/+ denote the *a priori/posteriori* estimates, and derivation of $\mathbf{h}_w(\boldsymbol{\vartheta}_w, \mathbf{u}_w)$ with respect to $\boldsymbol{\vartheta}_w$ is referred to as the sensitivity matrix and is calculated using the finite difference approach. The estimation method that is used in this study is referred as Extended Kalman filter (EKF) for parameter-only estimation [62]. In this method, the *a priori* estimates of the mean vector and covariance matrix of the unknown model parameters at each estimation window are considered equal to the *a posteriori* estimates at the previous estimation window. This is depicted in Eqs. (10) and (11). Moreover, the estimation problem is solved across each estimation window iteratively and the subscripts 0 and k in the following equations denote the iteration number.

$$\widehat{\boldsymbol{\vartheta}}_{w,0}^{-} = \widehat{\boldsymbol{\vartheta}}_{w-1}^{+} \tag{10}$$

$$\widehat{\mathbf{P}}_{\boldsymbol{\vartheta}\boldsymbol{\vartheta},w,0}^{-} = \widehat{\mathbf{P}}_{\boldsymbol{\vartheta}\boldsymbol{\vartheta},w-1}^{+} \tag{11}$$

The term $\widehat{\mathbf{P}}_{\boldsymbol{\vartheta}\boldsymbol{\vartheta},w}^{-/+}$ is the *a priori/posteriori* estimate of the covariance matrix of the unknown model parameters at the w^{th} estimation window. For the sake of brevity, the details for the derivation of the Bayesian inference based on the EKF method is not shown here and only the recursive equations at each estimation window are presented. After completing the iteration process at each estimation window, the estimation moves to the next window and the process is repeated. To complete the iteration process at each estimation window, the estimates of unknown model parameters needs to be converged. However, to improve the efficiency of the process, the maximum number of iterations is limited. More details are available in [62].

$$\widehat{\boldsymbol{\vartheta}}_{w,k+1}^{-} = \widehat{\boldsymbol{\vartheta}}_{w,k}^{+} \tag{12}$$

$$\widehat{\mathbf{P}}_{\boldsymbol{\vartheta}\boldsymbol{\vartheta},w,k+1}^{-} = \widehat{\mathbf{P}}_{\boldsymbol{\vartheta}\boldsymbol{\vartheta},w,k}^{+} + \mathbf{Q}_w \tag{13}$$

$$\widehat{\boldsymbol{\vartheta}}_{w,k+1}^{+} = \widehat{\boldsymbol{\vartheta}}_{w,k+1}^{-} + \mathbf{K}_{w,k+1}\left(\mathbf{y}_w - \hat{\mathbf{y}}_{w,k+1}^{-}\right) \tag{14}$$

$$\widehat{\mathbf{P}}_{\boldsymbol{\vartheta}\boldsymbol{\vartheta},w,k+1}^{+} = \left(\mathbf{I} - \mathbf{K}_{w,k+1}\mathbf{C}_{w,k+1}\right)\widehat{\mathbf{P}}_{\boldsymbol{\vartheta}\boldsymbol{\vartheta},w,k+1}^{-}\left(\mathbf{I} - \mathbf{K}_{w,k+1}\mathbf{C}_{w,k+1}\right)^{T} + \mathbf{K}_{w,k+1}\mathbf{R}_w{\mathbf{K}_{w,k+1}}^{T} \tag{15}$$

while,

$$\mathbf{K}_{w,k+1} = \widehat{\mathbf{P}}_{\boldsymbol{\vartheta}\mathbf{y},w,k+1}^{-}\left(\widehat{\mathbf{P}}_{\mathbf{y}\mathbf{y},w,k+1}^{-}\right)^{-1} \tag{16}$$

$$\mathbf{C}_{w,k+1} = \frac{\partial\, \mathbf{h}_w(\boldsymbol{\vartheta}, \mathbf{u}_w)}{\partial\, \boldsymbol{\vartheta}^T}\Big|_{\boldsymbol{\vartheta}=\widehat{\boldsymbol{\vartheta}}_{w,k+1}^{-}} \tag{17}$$

$$\widehat{\mathbf{P}}_{\mathbf{y}\mathbf{y},w,k+1}^{-} = \mathbf{C}_{w,k+1}\widehat{\mathbf{P}}_{\boldsymbol{\vartheta}\boldsymbol{\vartheta},w,k+1}^{-}{\mathbf{C}_{w,k+1}}^{T} + \mathbf{R}_w \tag{18}$$

$$\widehat{\mathbf{P}}_{\boldsymbol{\vartheta}\mathbf{y},w,k+1}^{-} = \widehat{\mathbf{P}}_{\boldsymbol{\vartheta}\boldsymbol{\vartheta},w,k+1}^{-}{\mathbf{C}_{w,k+1}}^{T} \tag{19}$$

The term $\mathbf{Q}_w \in \mathbb{R}^{n_{\vartheta B}\times n_{\vartheta B}}$ is the covariance matrix for the process noise ($\mathbf{q}_w \sim N(0, \mathbf{Q}_w)$). The matrix $\mathbf{Q}_w$ is a diagonal matrix and its j^{th} diagonal entry is equal to q times the j^{th} entry in vector $\widehat{\boldsymbol{\vartheta}}_w^{-}$. The term q is set equal to 0.002. The term $\mathbf{R}_w \in \mathbb{R}^{(t_w\times n_y)\times(t_w\times n_y)}$ is the measurement noise ($\boldsymbol{\lambda}_w \sim N(0, \mathbf{R}_w)$) and is modeled as a block diagonal matrix with the simulation error covariance matrix – including measurement noise – on the diagonal blocks. In this study, the diagonal entries of the matrix $\mathbf{R}_w$ are set equal to $(0.32\%g)^2$ at all measurement channels. The value $0.32\%g$ is approximately equal to the average root-mean-square of ambient measurements. The term $\hat{\mathbf{y}}_{w,k+1}^{-}$ is the *a priori* FE-predicted response calculated at $\widehat{\boldsymbol{\vartheta}}_{w,k+1}^{-}$. The matrix $\mathbf{K}_{w,k+1} \in \mathbb{R}^{n_{\vartheta B}\times(t_w\times n_y)}$ is the Kalman-gain matrix at the $(k+1)^{\text{th}}$ iteration in the w^{th} estimation window. The matrix $\mathbf{C}_{w,k+1} \in \mathbb{R}^{(t_w\times n_y)\times n_{\vartheta B}}$ is the FE response sensitivity matrix – with respect to $\widehat{\boldsymbol{\vartheta}}_{w,k+1}^{-}$ – at the $(k+1)^{\text{th}}$ iteration in the w^{th} estimation window. The term $\mathbf{I} \in \mathbb{R}^{n_{\vartheta B}\times n_{\vartheta B}}$ denotes the identity matrix. The matrix $\widehat{\mathbf{P}}_{\mathbf{y}\mathbf{y},w,k+1}^{-} \in \mathbb{R}^{(t_w\times n_y)\times(t_w\times n_y)}$ is *a priori* estimate of the covariance matrix of $\hat{\mathbf{y}}_{w,k+1}^{-}$, and $\widehat{\mathbf{P}}_{\boldsymbol{\vartheta}\mathbf{y},w,k+1}^{-} \in \mathbb{R}^{n_{\vartheta B}\times(t_w\times n_y)}$ is the *a priori* estimate of the cross-covariance matrix of $\widehat{\boldsymbol{\vartheta}}_{w,k+1}^{-}$ and $\hat{\mathbf{y}}_{w,k+1}^{-}$. The matrix $\widehat{\mathbf{P}}_{\boldsymbol{\vartheta}\boldsymbol{\vartheta},0}^{+}$ is initialized diagonally with diagonal entries equal to the initial variance of the initial estimate of the unknown model parameters. The j^{th} diagonal entry in $\widehat{\mathbf{P}}_{\boldsymbol{\vartheta}\boldsymbol{\vartheta},0}^{+}$ is equal to the square of p_ϑ times the j^{th} entry in vector $\widehat{\boldsymbol{\vartheta}}_0^{+}$. In this study p_ϑ is set equal to 0.1. The recursive Bayesian model updating process in each estimation window is completed after 10 iterations or

Preprints (www.preprints.org) | NOT PEER-REVIEWED | Posted: 15 December 2022 doi:10.20944/preprints202212.0282.v1

meeting the following convergence criteria in the posterior estimates of unknown model parameters.

$$\left|\hat{\vartheta}^{+}_{w,k+1} - \hat{\vartheta}^{+}_{w,k}\right| < (0.02) \times \left|\hat{\vartheta}^{+}_{w,k}\right| \tag{20}$$

6.3. Results

This section presents the second step of the introduced two-step model updating approach and its application for damage identification of the testbed structure. First, the Bayesian model updating is carried out and its performance is discussed through the updating process of unknown model parameters and the fit between measurements and posterior estimates of FE-predicted responses. Subsequently, the final estimates of unknown model parameters are used to infer damage in the girders and calculate the overall damping of the testbed structure. To assess the application of Bayesian FE model updating, the data sets presented in Table 4 are used. As explained in Section 6.1, while the excitation frequencies close to the first two modes are lumped together, the target load amplitudes and layouts differ from one data set to another one. As mentioned before, lumping the frequencies together increases the identifiability of model parameters and the parameter estimation stability by using the dynamic response behavior of testbed structure from its two first vertical modes.

The updating process for the posterior estimates of the unknown model parameters $f'_{c,W}$, $f'_{c,E}$, ξ_1, ξ_2, and C_D using data of Table 4 is shown in Figure 11. In this figure, the estimates of the unknown model parameters are normalized to the corresponding initial values. As can be seen in this figure, all the unknown model parameters are updated from their initial values and smoothly converged to their final estimates.

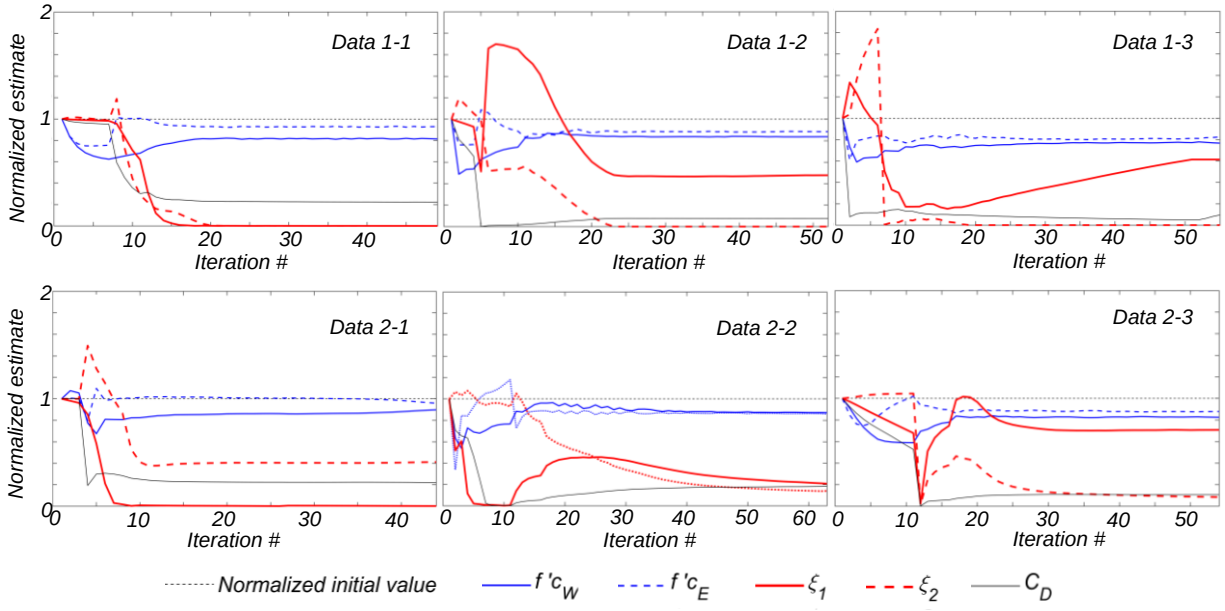

Figure 11. Updating process for the posterior estimates of the unknown model parameters using data in Table 4.

Next, the prior estimates of responses – simulated responses using the prior FE model – and the posterior ones are compared with the field measurements. For the sake of brevity, only one second of data obtained using Data 1-2 are shown in Figure 12. In this figure, the two top rows correspond to channels 1 to 10 and the excitation frequency of 9.73 Hz, and the two bottom rows correspond to the same channels and the excitation frequency of 12.86 Hz. For the case of excitation frequency of 9.73 Hz, the prior FE responses mostly underestimate the measurements in channels located between the supports (channels 2, 3, 4, 7, 8, and 9), and slightly overestimate the responses in channels located on the overhang parts (channels 1, 5, 6, and 10). However, the responses in all channels are initially overestimated for the excitation frequency of 12.86 Hz. This shows that although the prior

Preprints (www.preprints.org) | NOT PEER-REVIEWED | Posted: 15 December 2022 doi:10.20944/preprints202212.0282.v1

FE model matches the main modal signatures of the real structure, it cannot correctly predict the measurements in the time domain. As can be seen in Figure 12, after the application of Bayesian model updating, the updated FE model better fits the measurement responses in time domain. This improvement is noticeable in various channels and for both excitation frequencies of 9.73 Hz and 12.86 Hz.

To quantify the discrepancies between two signals, the relative root mean square error (RRMSE) is calculated as follow.

$$\text{RRMSE}(\%) = \frac{\sqrt{\sum_{i=t_1}^{t_n}(\hat{\mathbf{s}}_i - \mathbf{s}_i)^2}}{\sqrt{\sum_{i=t_1}^{t_n}(\mathbf{s}_i)^2}} \times 100 \tag{21}$$

In the above equation, $\mathbf{s}_i$ and $\hat{\mathbf{s}}_i$ denotes the measured and estimated responses at the i^{th} time step. The closer the RRMSE gets to zero, the better signals $\mathbf{s}$ and $\hat{\mathbf{s}}$ match. The RRMSEs are calculated between the measured responses and their prior/posterior FE-predicted responses and are listed in Table 5.

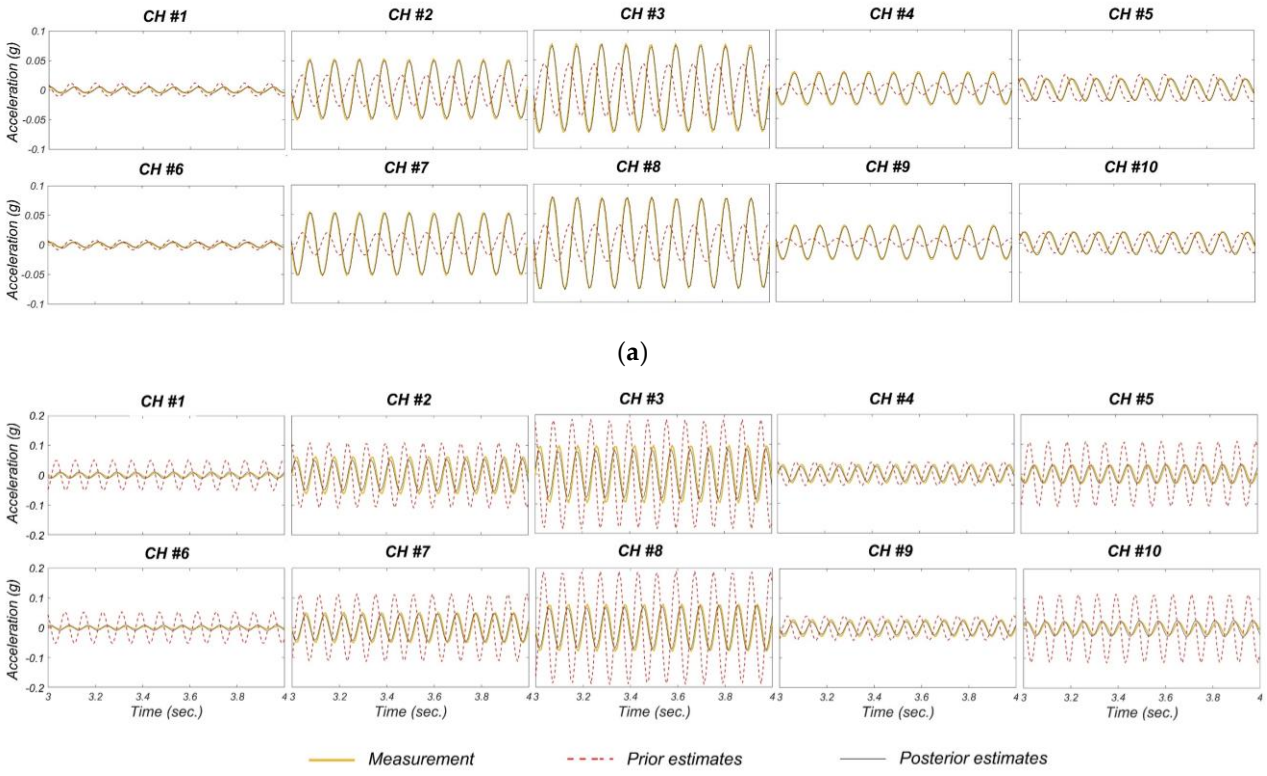

(**a**)

(**b**)

Figure 12. The measured, prior and posterior estimates of FE-predicted responses using Bayesian FE model updating based on Data 1-2: (**a**) excitation frequency of 9.73 Hz, and (**b**) excitation frequency of 12.86 Hz.

Preprints (www.preprints.org) | NOT PEER-REVIEWED | Posted: 15 December 2022 doi:10.20944/preprints202212.0282.v1

Table 5. RRMSEs (%) between the measurements and FE-predicted responses from the prior and posterior model.

Data I.D.	CH #	9.73Hz excitation frequency										12.86Hz excitation frequency									
		1	2	3	4	5	6	7	8	9	10	1	2	3	4	5	6	7	8	9	10
1-1	Prior	201	75	74	80	66	170	76	74	83	46	161	63	63	70	67	202	67	68	72	97
	Posterior	172	14	9	22	27	192	22	17	28	28	132	16	15	22	40	153	11	11	23	57
1-2	Prior	163	107	110	102	127	119	101	102	99	101	300	112	117	103	164	565	133	140	109	269
	Posterior	24	11	10	10	22	34	10	9	8	21	72	23	24	24	30	133	20	21	13	55
1-3	Prior	191	128	134	116	165	137	114	118	108	130	429	146	156	126	235	1111	193	205	141	480
	Posterior	24	11	12	20	21	46	11	13	18	18	90	33	35	35	41	254	27	28	20	93
2-1	Prior	312	61	58	71	55	259	63	60	75	30	590	30	27	46	124	236	30	26	51	84
	Posterior	191	8	8	18	46	213	17	14	23	50	312	7	4	22	68	133	9	9	22	54
2-2	Prior	229	78	78	84	66	187	78	77	85	40	388	54	52	64	80	250	55	54	66	117
	Posterior	139	11	9	20	46	172	18	15	20	60	236	7	7	17	65	175	9	7	26	72
2-3	Prior	109	611	64	46	114	104	62	66	43	128	124	38	34	36	17	54	33	33	49	33
	Posterior	83	8	7	17	52	99	12	11	11	61	180	9	10	13	49	177	10	9	21	82

As can be seen in Table 5, RRMSE values are reduced from prior to posterior values for all measurement channels. This shows that the time-domain model updating reduces the discrepancies between FE-predicted and measured responses successfully. However, the highest posterior RRMSEs are due to channels 1, 5, 6 and 10. These channels are located on the overhang parts of the girders (see Figure 4) and the measurements are likely less reliable due to the low signal-to-noise ratio. It is understandable from Figure 12 and Table 5 that the FE-predicted responses at these channels are promisingly updated to match the measurements.

The final estimates of unknown model parameters using all data are shown in Figure 13. The average final estimates of parameters $f'_{c,W}$ and $f'_{c,E}$ are approximately 30% and 26% less than their initial values. Previous studies [63,64] have shown more than 25% reductions in concrete compressive strength of deteriorated concrete structures—e.g., abandoned structures and structures in acidic environments. Considering that the operating environment of girders caused them to be prone to various damage mechanisms (including concrete degradation, as well as steel corrosion as discussed in Section 2.1) the final estimates of parameters $f'_{c,W}$ and $f'_{c,E}$ are reasonable. Moreover, as mentioned in Section 2.1, after being decommissioned, the west girder has been under more intense environmental testing conditions than the east girder [36]. This can be understood from the model updating results as the final estimates of parameter $f'_{c,W}$ is smaller than $f'_{c,E}$. The only exception is the case study with Data 2-1 in which the final estimate of $f'_{c,E}$ is smaller than $f'_{c,W}$. This is most probably an estimation error due to measurement noise, experimental error, etc. Moreover, based on Figure 13 and ignoring the case study with Data 2-1, the maximum difference in the estimation of parameter f'_c in layouts 1 and 2 is less than 7% which shows the consistency of Bayesian model updating results regardless of the shaker location and target load amplitude.

Preprints (www.preprints.org) | NOT PEER-REVIEWED | Posted: 15 December 2022 doi:10.20944/preprints202212.0282.v1

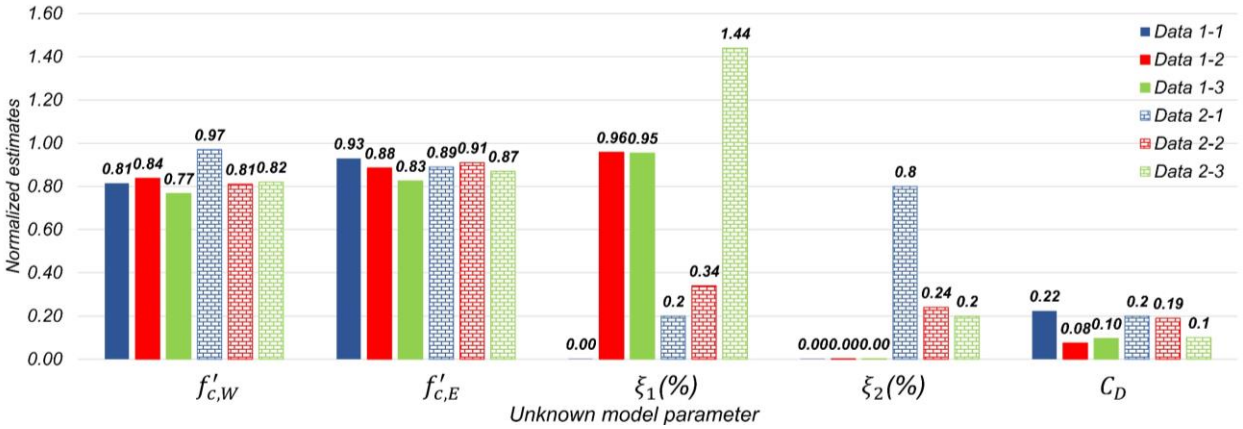

Figure 13. The final estimates of unknown model parameters using data sets in Table 4. The information on each set of data are shown in Table 4.

The final estimates for modal damping parameters vary between different data sets. The identifiability analysis showed dependencies between parameters ξ_1, ξ_2, and C_D. This dependency is most probably a reason for the discrepancy between the final estimates of these parameters using different data sets. Aside from this, it is known that structural damping roots in various factors including opening and closing of micro cracks, friction in structural joints, level of vibration, and other sources of energy dissipation, etc. [65,66]. These conditions could be varied from one experiment to another and result in different level of damping. To have insight into the overall damping of the testbed structure, the modal damping ratios are calculated using the state matrix of the system. For this purpose, the stiffness, mass and damping matrices of the system are developed for the posterior models. The stiffness (**K**) matrix is recorded as current global system matrix (using OpenSees *printA* command) while a static analysis using *LoadControl* integrator is carried out and damping is removed from the model. The mass matrix (**M**) is calculated based on the current global system matrix while a static analysis using *LoadControl* integrator and a transient analysis using *CentralDifference* integrator is carried out and damping is removed from the model. Using the Central Difference formulation presented in Eq. (22), the mass matrix is equal to the recorded current global system matrix ($\widehat{\mathbf{K}}_{CDF}$) times Δt^2. In Eq. (22), the term Δt is the size of time step increment and is set to a very small value (here 10^{-6} second) to record the current global system matrix with high precision. The term **C** is the damping matrix.

$$\widehat{\mathbf{K}}_{CDF} = \frac{\mathbf{M}}{(\Delta t)^2} + \frac{\mathbf{C}}{2\Delta t} \tag{22}$$

Including damping in the model and carrying out a transient analysis using Newmark integrator with $\gamma = 0.5$ and $\beta = 0.25$, the matrix $\widehat{\mathbf{K}}_{Newmark}$ can be recorded using *printA*. The damping matrix is calculated as it is shown in Eq. (23) using the Newmark formulation.

$$\mathbf{C} = \frac{\beta\ \Delta t}{\gamma}\ (\widehat{\mathbf{K}}_{Newmark} - \mathbf{K} - \frac{\mathbf{M}}{\beta\ (\Delta t)^2}) \tag{23}$$

The matrices **M**, **C** and **K** are condensed at the dynamic DOFs and the state matrix is calculated [65]. Using the state matrix of the posterior models, the modal damping ratios are obtained for all data sets. These damping ratios are reported in Figure 14. As can be seen, the testbed structure dissipates a greater level of energy in its first mode than in the second mode which agrees with the identified modal damping ratios (see Table 1). Moreover, the overall modal damping ratios estimated from experiments with larger target load amplitudes are smaller than those estimated from experiments with smaller target load amplitudes. Although this has been previously observed in a few system identification studies [67,68], it is in contrast with the literature in which damping increases as load amplitude increases.

Preprints (www.preprints.org) | NOT PEER-REVIEWED | Posted: 15 December 2022 doi:10.20944/preprints202212.0282.v1

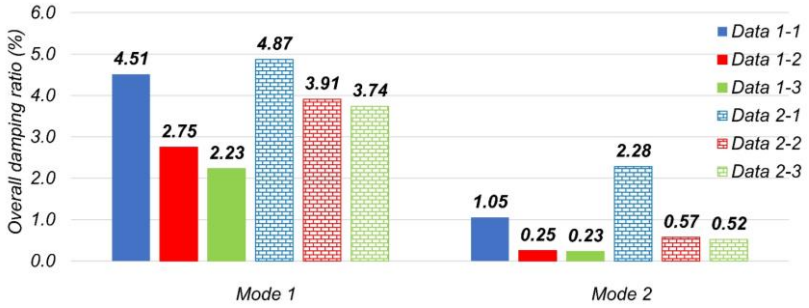

Figure 14. Overall damping ratio of the testbed structure for mode 1 and mode 2 using different data sets.

7. Conclusions

This study presented a two-step finite element (FE) model updating approach for the purpose of operational health monitoring and damage identification of bridge structures using acceleration measurements. In this approach, first, modal-based model updating is carried out to calibrate the initial FE model of the bridge developed using as-built drawings. In this step, the uncertain model parameters are updated to fit the FE-predicted and identified modal signatures of the bridge. Modal properties are sensitive to parameters that characterize the linear response behavior of the structure. Based on this, stiffness-related model parameters – mainly related to boundary conditions – as well as initial stiffness of concrete material are estimated at this step. However, it is well-known that concrete material has nonlinear response behavior even under very small level of stress. In addition, presence of prestressing force in concrete bridges – which is a conventional solution to improve the flexural strength of girder's section – pushes the concrete material far in its nonlinear response curve. To account for the nonlinear response behavior of bridge and/or its structural components as well as refinement of model parameter estimation, Bayesian time-domain model updating – referred here as the second step of model updating procedure – is carried out to estimate the material properties that reflect the cumulative damage in the bridge, e.g., effective concrete compressive strength. To prevent convergence of model updating algorithm to the local solution, the initial values for concrete compressive strength are selected using the final estimates of concrete initial stiffness from modal-based model updating. The linear-elastic boundary conditions are fixed at their final estimates using modal-based model updating. Moreover, the damping energy-dissipation-related model parameters are also considered to be estimated using time-domain model updating. Updating the uncertain model parameters in two steps reduces the challenges of the model updating process due to the modeling error, ill-conditioning, unidentifiability, and/or mutual dependency of model parameters.

The application of the two-step model updating approach was presented for a pair of full-scale precast prestressed bridge I-girders as the testbed structure. These girders were in service for 40 years until they were decommissioned and transferred to the Turner-Fairbank Highway Research Center (TFHRC) in McLean, Virginia. At the time of this study, these girders were significantly deteriorated. For this study, a series of forced-vibration experiments were planned and the testbed structure was subjected to sinusoidal force excitations through frequency sweeps at three different amplitudes using a small shaker. The input excitation was measured using load cells and the acceleration responses were collected using a wireless sensing network.

Modal identification was carried out using forced-vibration experimental data. Then, the initial FE model of the testbed was developed in OpenSees using the as-built drawings. It was expected to have a considerable level of uncertainty in this initial model with respect to boundary conditions and material properties. To calibrate this model, first, a modal-based model updating was carried out and linear model parameters – e.g.,

stiffness of supports and modulus of elasticity of concrete – were estimated. In the next step, Bayesian time-domain model updating was performed to refine the estimates for concrete compressive strength of girders and estimate the damping energy-dissipation-related model parameters. The final estimates of concrete compressive strength showed up to 30% reduction compared to the nominal values, which based on literature is a realistic quantification of damage for highly deteriorated and aged concrete components. Although the input load in this study was different from the traffic load during the operation of bridges, it provided a real-world exercise to validate the capability of the two-step model updating approach for damage identification of bridge structures.

Author Contributions

Conceptualization, F.G. and H.E.; methodology, N.M., F.G., and H.E.; software, N.M. and F.G.; validation, N.M., F.G. and H.E.; formal analysis, N.M. and F.G.; investigation, N.M., F.G. and H.E.; resources, H.E., M.B., and E.T.; data curation, N.M., M.B. and E.A.; writing—original draft preparation, N.M.; writing—review and editing, N.M., F.G., H.E., M.B., and E.T.; visualization, N.M.; supervision, H.E., and E.T.; project administration, H.E. and M.B.; funding acquisition, H.E., and M.B.. All authors have read and agreed to the published version of the manuscript.

Funding

This project was funded through the United States Department of Transportation Small Business Innovative Research (SBIR) program Phase II (Contract #6913G619C100048). The project resulted from the collaboration between S.C. Solutions, Inc., the leading small business, the University of California Los Angeles (UCLA), and the University of Nevada, Reno. Opinions and findings in this study are those of the authors and do not necessarily reflect the views of the sponsor.

Data Availability Statement

Data and materials supporting the results or analyses presented in this work are available upon reasonable request from the corresponding author.

Acknowledgments

Authors would like to acknowledge Dr. Hoda Azari (FHWA NDE Center) for making available the prestressed girder testbed at the Turner Fairbank Highway Research Center, and Mr. Blake Cox (FHWA NDE Center) who aided during testing.

Conflicts of Interest

The authors declare no conflict of interest.

References

[1] ASCE, ASCE's 2021 infrastructure report card, 2021. https://infrastructurereportcard.org/cat-item/bridges/.

[2] M. Friswell, J.E. Mottershead, Finite element model updating in structural dynamic, Springer Science+Business Media, Berlin, 1995. https://doi.org/10.1007/9788-94-015-8508-8.

[3] J.L. Zapico, M.P. González, M.I. Friswell, C.A. Taylor, A.J. Crewe, Finite element model updating of a small scale bridge, J. Sound Vib. 268 (2003) 993–1012. https://doi.org/10.1016/S0022-460X(03)00409-7.

[4] X. Xiao, Y.L. Xu, Q. Zhu, Multiscale modeling and model updating of a cable-stayed bridge. II: model updating using modal frequencies and influence lines, J. Bridg. Eng. 20 (2015) 1–12. https://doi.org/10.1061/(asce)be.1943-5592.0000723.

[5] S. Kim, N. Kim, Y.S. Park, S.S. Jin, A sequential framework for improving identifiability of FE model updating using static and dynamic data, Sensors (Switzerland). 19 (2019) 5099. https://doi.org/10.3390/s19235099.

[6] Y. Li, R. Astroza, J.P. Conte, P. Soto, Nonlinear FE model updating of seismic isolated bridge instrumented during the 2010 Mw 8.8 Maule-Chile Earthquake, Procedia Eng. 199 (2017) 3003–3008. https://doi.org/10.1016/j.proeng.2017.09.397.

[7] E. Taciroglu, A. Shamsabadi, F. Abazarsa, R.L. Nigbor, S.F. Ghahari, Comparative study of model predictions and data from the Caltrans-CSMIP bridge instrumentation program: A case study on the Eureka-Samoa channel bridge., Sacramento, 2014. https://doi.org/10.13140/RG.2.1.1555.0164.

[8] A. Teughels, G. De Roeck, Structural damage identification of the highway bridge Z24 by FE model updating, J. Sound Vib. 278 (2004) 589–610. https://doi.org/10.1016/j.jsv.2003.10.041.

[9] H. Schlune, M. Plos, K. Gylltoft, Improved bridge evaluation through finite element model updating using static and dynamic measurements, Eng. Struct. 31 (2009) 1477–1485. https://doi.org/10.1016/j.engstruct.2009.02.011.

[10] C. Costa, A. Arêde, A. Costa, E. Caetano, A. Cunha, F. Magalhaes, Updating numerical models of masonry arch bridges by operational modal analysis, Int. J. Archit. Herit. 9 (2015) 760–774. https://doi.org/10.1080/15583058.2013.850557.

[11] L. He, E. Reynders, J.H. García-Palacios, G.C. Marano, B. Briseghella, G. De Roeck, Wireless-based identification and model updating of a skewed highway bridge for structural health monitoring, Appl. Sci. 10 (2020) 2347. https://doi.org/10.3390/app10072347.

[12] H. Tran-Ngoc, S. Khatir, G. De Roeck, T. Bui-Tien, L. Nguyen-Ngoc, M. Abdel Wahab, Model updating for nam O bridge using particle swarm optimization algorithm and genetic algorithm, Sensors (Switzerland). 18 (2018) 4131. https://doi.org/10.3390/s18124131.

[13] J.E. Mottershead, M.I. Friswell, Model updating in structural dynamics: A survey, J. Sound Vib. 167 (1993) 347–375. https://doi.org/10.1006/jsvi.1993.1340.

[14] F. Ghahari, N. Malekghaini, H. Ebrahimian, E. Taciroglu, Bridge digital twinning using an output-only Bayesian model updating method and recorded seismic measurements, Sensors. 22 (2022) 1278. https://doi.org/https://doi.org/10.3390/s22031278.

[15] M. Abedin, F.J. De Caso y Basalo, N. Kiani, A.B. Mehrabi, A. Nanni, Bridge load testing and damage evaluation using model updating method, Eng. Struct. 252 (2022) 113648. https://doi.org/10.1016/j.engstruct.2021.113648.

[16] F. Magalhães, Á. Cunha, E. Caetano, Online automatic identification of the modal parameters of a long span arch bridge, Mech. Syst. Signal Process. 23 (2009) 316–329. https://doi.org/10.1016/j.ymssp.2008.05.003.

[17] J.-N. Juang, Applied system identification, Prentice Hall, Englewood Cliffs, 1994.

[18] G.H. James, III, T.G. Carne, J.P. Lauffer, The natural excitation technique (NExT) for modal parameter extraction from operating wind turbines, United States, 1993. https://www.osti.gov/biblio/10139203.

[19] L. Ljung, System identification theory for the user, 2nd ed., Prentice Hall PTR, New Jersey, 1999.

[20] D.J. Ewins, Modal testing: theory, practice and application, 2nd ed., John Wiley & Sons, Hoboken, 2009.

[21] M.I. Friswell, J.E. Mottershead, Finite element model updating in structural dynamics, Springer, New York City, 1995. https://link.springer.com/book/10.1007/978-94-015-8508-8.

[22] B. Moaveni, X. He, J.P. Conte, J.I. Restrepo, Damage identification study of a seven-story full-scale building slice tested on the UCSD-NEES shake table, Struct. Saf. 32 (2010) 347–356. https://doi.org/10.1016/j.strusafe.2010.03.006.

[23] C.R. Farrar, W.E. Baker, T.M. Bell, K.M. Cone, T.W. Darling, T.A. Duffey, A. Eklund, A. Migliori, Dynamic characterization and damage detection in the I-40 bridge over the Rio Grande, Los Alamos. LA-12767-M (1994) 1–153.

[24] C. Farrar, P. Cornwell, Structural health monitoring studies of the Alamosa Canyon and I-40 bridges, (2000). https://doi.org/10.2172/766805.

[25] Y. Zheng, H. Wu, X. You, H. Xie, Model updating-based dynamic collapse analysis of a RC cable-stayed bridge under earthquakes, Structures. 43 (2022) 1100–1113. https://doi.org/10.1016/j.istruc.2022.07.023.

[26] H. Ebrahimian, R. Astroza, J.P. Conte, C. Papadimitriou, Bayesian optimal estimation for output-only nonlinear system and damage identification of civil structures, Struct. Control Heal. Monit. 25 (2018) 1–32. https://doi.org/10.1002/stc.2128.

[27] X. Zhou, C.W. Kim, F.L. Zhang, K.C. Chang, Vibration-based Bayesian model updating of an actual steel truss bridge subjected to incremental damage, Eng. Struct. 260 (2022) 114226. https://doi.org/10.1016/j.engstruct.2022.114226.

[28] C. Fang, H.J. Liu, H.F. Lam, M.O. Adeagbo, H.Y. Peng, Practical model updating of the Ting Kau bridge through the MCMC-

based Bayesian algorithm utilizing measured modal parameters, Eng. Struct. 254 (2022) 113839. https://doi.org/10.1016/j.engstruct.2022.113839.

[29] Z. Xia, A. Li, J. Li, H. Shi, M. Duan, G. Zhou, Model updating of an existing bridge with high-dimensional variables using modified particle swarm optimization and ambient excitation data, Meas. J. Int. Meas. Confed. 159 (2020) 107754. https://doi.org/10.1016/j.measurement.2020.107754.

[30] S.S. Saidin, S.A. Kudus, A. Jamadin, M.A. Anuar, N.M. Amin, Z. Ibrahim, A.B. Zakaria, K. Sugiura, Operational modal analysis and finite element model updating of ultra-high-performance concrete bridge based on ambient vibration test, Case Stud. Constr. Mater. 16 (2022) e01117. https://doi.org/10.1016/j.cscm.2022.e01117.

[31] W. Fan, P. Qiao, Vibration-based damage identification methods: A review and comparative study, Struct. Heal. Monit. 10 (2011) 83–111. https://doi.org/10.1177/1475921710365419.

[32] L. Luo, Finite element model updating method for continuous girder bridges using monitoring responses and traffic videos, 29 (2022) e3062. https://doi.org/10.1002/stc.3062.

[33] S.Z. Chen, Q.M. Zhong, S.T. Hou, G. Wu, Two-stage stochastic model updating method for highway bridges based on long-gauge strain sensing, Structures. 37 (2022) 1165–1182. https://doi.org/10.1016/j.istruc.2022.01.082.

[34] M.K. Ramancha, R. Astroza, R. Madarshahian, J.P. Conte, Bayesian updating and identifiability assessment of nonlinear finite element models, Mech. Syst. Signal Process. 167 (2022) 108517. https://doi.org/10.1016/j.ymssp.2021.108517.

[35] E. Yu, E. Taciroglu, J.W. Wallace, Parameter identification of framed structures using an improved finite element model-updating method — Part I : Formulation and verification, 36 (2007) 619–639. https://doi.org/10.1002/eqe.

[36] N. Gucunski, S.K. Lee, C. Mazzotta, S.H. Kee, B. Pailes, F. Fetrat, Protocols for condition assessment of prestressed concrete girders using NDE and physical testing, Washington D.C., 2014.

[37] U.S. Department of transportation, federal highway administration, (2020). https://highways.dot.gov/research/turner-fairbank-highway-research-center/facility-overview.

[38] M. Adams, J. Nicks, T. Stabile, Thermal activity of geosynthetic reinforced soil piers, in: IFCEE, ASCE, San Antonio, 2015. https://doi.org/https://doi.org/10.1061/9780784479087.241.

[39] P. C. LIU, Damage to concrete structures in a marine environment, Mater. Struct. 24 (1997) 302–307. https://doi.org/https://doi.org/10.1007/BF02472086.

[40] Parker Lord, (2022). https://www.microstrain.com/.

[41] SensorConnect, (2022). https://www.microstrain.com/software/sensorconnect.

[42] S.A. Fulop, K. Fitz, Algorithms for computing the time-corrected instantaneous frequency (reassigned) spectrogram, with applications, J. Acoust. Soc. Am. 119 (2006) 360–371. https://doi.org/10.1121/1.2133000.

[43] P.D. Welch, The use of the fast fourier transform for the estimation of power spectra: a method based on time averaging over short, modified periodograms, IEEE Trans. Audio Electroacoust. 15 (1967) 70–73. https://doi.org/10.1109/TAU.1967.1161901.

[44] P. Overschee, B. Moor, Subspace identification for linear systems theory — implementation — applications, Kluwer Academic Publishers, Dordrecht, 1996. https://doi.org/10.1007/978-1-4613-0465-4.

[45] B. Peeters, G. De Roeck, Reference based stochastic subspace identification in Civil Engineering, Inverse Probl. Eng. 8 (2000) 47–74. https://doi.org/10.1080/174159700088027718.

[46] MathWorks, n4sid estimate state-space model, (2022). https://www.mathworks.com/help/ident/ref/n4sid.html.

[47] J.B. Bodeux, J.C. Golinval, Application of ARMAV models to the identification and damage detection of mechanical and civil engineering structures, Smart Mater. Struct. 10 (2001) 479–489. https://doi.org/10.1088/0964-1726/10/3/309.

[48] MathWorks, sset estimate state-space mode, (n.d.). https://www.mathworks.com/help/ident/ref/ssest.html.

[49] F. McKenna, OpenSees: A framework for earthquake engineering simulation, Comput. Sci. Eng. 13 (2011) 58–66. https://doi.org/10.1109/MCSE.2011.66.

[50] F. Naeim, J. Kelly, Design of seismic isolated structures: from theory to practice, John Wiley & Sons, New York, 1999.

[51] A.K. Chopra, Dynamics of structures, Fourth, Prentice Hall, Englewood Cliffs, 1995.

[52] M.S. Nabiyan, F. Khoshnoudian, B. Moaveni, H. Ebrahimian, Mechanics-based model updating for identification and virtual sensing of an offshore wind turbine using sparse measurements, Struct. Control Heal. Monit. 28 (2021). https://doi.org/10.1002/stc.2647.

[53] MathWorks, Matlab R2019a, (2019).

[54] MathWorks, fmincon Algorithms, (2022). https://www.mathworks.com/help/optim/ug/choosing-the-algorithm.html.

[55] K. Van Den Abeele, Damage assessment in reinforced concrete using nonlinear vibration techniques, 30 (2003) 341–344. https://doi.org/10.1063/1.1309237.

[56] N. Gucunski, A. Imani, F. Romero, S. Nazarian, D. Yuan, H. Wiggenhauser, P. Shokouhi, A. Taffe, D. Kutrubes, Nondestructive testing to identify concrete bridge deck deterioration, Washington D.C., 2013. https://nap.nationalacademies.org/catalog/22771/nondestructive-testing-to-identify-concrete-bridge-deck-deterioration.

[57] I. Fernandez, M.F. Herrador, A.R. Marí, J.M. Bairán, Structural effects of steel reinforcement corrosion on statically indeterminate reinforced concrete members, Mater. Struct. Constr. 49 (2016) 4959–4973. https://doi.org/10.1617/s11527-016-0836-2.

[58] W. Zhu, Effect of corrosion on the mechanical properties of the corroded reinforcement and the residual structural performance of the corroded beams, Universite de Toulouse, 2015. https://tel.archives-ouvertes.fr/tel-01222175/document.

[59] H. Ebrahimian, R. Astroza, J.P. Conte, R.R. Bitmead, Information-theoretic approach for identifiability assessment of nonlinear structural finite-element models, J. Eng. Mech. 145 (2019) 1–14. https://doi.org/10.1061/(ASCE)EM.1943-7889.0001590.

[60] M. Song, R. Astroza, H. Ebrahimian, B. Moaveni, C. Papadimitriou, Adaptive Kalman filters for nonlinear finite element model updating, Mech. Syst. Signal Process. 143 (2020) 106837. https://doi.org/10.1016/j.ymssp.2020.106837.

[61] H. Ebrahimian, M. Kohler, A. Massari, D. Asimaki, Parametric estimation of dispersive viscoelastic layered media with application to structural health monitoring, Soil Dyn. Earthq. Eng. 105 (2018) 204–223. https://doi.org/10.1016/j.soildyn.2017.10.017.

[62] H. Ebrahimian, R. Astroza, J.P. Conte, Extended Kalman filter for material parameter estimation in nonlinear structural finite element models using direct differentiation method, Earthq. Eng. Struct. Dyn. 44 (2015) 1495–1522. https://doi.org/10.1002/eqe.2532.

[63] M. Ismail, B. Muhammad, M.E.G. Ismail, Compressive strength loss and reinforcement degradations of reinforced concrete structure due to long-term exposure, Constr. Build. Mater. 24 (2010) 898–902. https://doi.org/10.1016/j.conbuildmat.2009.12.003.

[64] B. Li, L. Cai, K. Wang, Y. Zhang, Prediction of the residual strength for durability failure of concrete structure in acidic environments, J. Wuhan Univ. Technol. Mater. Sci. Ed. 31 (2016) 340–344. https://doi.org/10.1007/s11595-016-1373-0.

[65] C. Rainieri, G. Fabbrocino, E. Cosenza, Some remarks on experimental estimation of damping for seismic design of civil constructions, Shock Vib. 17 (2010) 383–395. https://doi.org/10.3233/SAV-2010-0534.

[66] C. Liang, T. Liu, J. Xiao, D. Zou, Q. Yang, The damping property of recycled aggregate concrete, Constr. Build. Mater. 102 (2016) 834–842. https://doi.org/10.1016/j.conbuildmat.2015.11.026.

[67] G.W. Chen, P. Omenzetter, S. Beskhyroun, Modal systems identification of an eleven-span concrete motorway off-ramp bridge using various excitations, Eng. Struct. 229 (2021) 111604. https://doi.org/10.1016/j.engstruct.2020.111604.

[68] J.M.W. Brownjohn, A.A. Dumanoglu, R.T. Severn, A. Blakeborough, Ambient vibration survey of the bosporus suspension bridge, Int. Assoc. Earthq. Eng. 18 (1989) 263–283. https://doi.org/10.1002/eqe.4290180210.